

## A DIRECT MEASUREMENT OF MAJOR GALAXY MERGERS AT $z \lesssim 3$

CHRISTOPHER J. CONSELICE,<sup>1,2</sup> MATTHEW A. BERSHADY,<sup>3</sup> MARK DICKINSON,<sup>4</sup>  
AND CASEY PAPOVICH<sup>5</sup>

Received 2003 April 14; accepted 2003 May 28

### ABSTRACT

This paper presents direct evidence for hierarchical galaxy assembly out to redshifts  $z \sim 3$ . We identify major mergers using the model-independent CAS (concentration, asymmetry, clumpiness) physical morphological system on galaxies detected, and photometrically selected, in the WFPC2 and NICMOS Hubble Deep Field North. We specifically use the asymmetric distributions of rest-frame optical light measured through the asymmetry parameter ( $A$ ) to determine the fraction of galaxies undergoing major mergers as a function of redshift ( $z$ ), stellar mass ( $M_*$ ), and absolute magnitude ( $M_B$ ). We find that the fraction of galaxies consistent with undergoing a major merger increases with redshift for all galaxies, but most significantly, at 5–10  $\sigma$  confidence, for the most luminous and massive systems. The highest merger fractions we find are 40%–50% for galaxies with  $M_B < -21$ , or  $M_* > 10^{10} M_\odot$  at  $z > 2.5$ , e.g., objects identified as Lyman-break galaxies. Using these results, we model the merger fraction evolution in the form  $f_m(A, M_*, M_B, z) = f_0 \times (1+z)^{m_A}$ . We find  $m_A$  values  $\sim 4$ – $6$  for the most luminous and massive galaxies, while lower mass and less luminous galaxies have smaller  $m_A$  values. We use these merger fractions, combined with merger timescales calculated from  $N$ -body simulations, to derive galaxy merger rates to  $z \sim 3$ . We also use stellar masses of HDF-N galaxies to determine the mass accretion rate of field galaxies involved in major mergers. We find an average stellar mass accretion rate of  $\dot{M}_G \sim 4 \times 10^8 M_\odot \text{ Gyr}^{-1}$  per galaxy at  $z \sim 1$  for galaxies with stellar masses  $M_* > 10^9 M_\odot$ . This accretion rate changes with redshift as  $\dot{M}_G = 1.6 \times 10^8 (1+z)^{0.99 \pm 0.32} M_\odot \text{ Gyr}^{-1}$  per galaxy. We also find that the fraction of stellar mass density in galaxies involved in major mergers increases with redshift, with a peak mass fraction  $\sim 0.5$  for the brightest,  $M_B < -21$ , and most massive,  $M_* > 10^{10} M_\odot$ , systems near  $z \sim 2.5$ . By comparing merger fractions predicted in cold dark matter semianalytic models with our results we find a reasonably good agreement for the largest and brightest systems, although we find more low-mass galaxy mergers at lower redshifts than what these models predict.

*Key words:* galaxies: evolution — galaxies: formation — galaxies: interactions

### 1. INTRODUCTION

There are two principal processes in galaxy formation: the assembly of mass, both baryonic and dark, through accretion and mergers, and the conversion of baryons into stars. While the latter process is now statistically mapped out to nearly the beginning of the universe using a variety of techniques (e.g., Lilly et al. 1996; Madau, Pozzetti, & Dickinson 1998), we are just beginning to understand the process and history of mass assembly. Furthermore, there are several types of mass assembly that are related in an unknown way, including the collapse, infall, and accretion of dark and baryonic matter, which are likely related to how baryonic material is converted into stars. Assembly of galaxies and dark halos through mergers and accretion is also potentially a major player in black hole and AGN evolution, the production of gravitational waves, the triggering of star formation, and possibly a driver of supernova and gamma-ray burst rates.

Hierarchical mass assembly is also the cornerstone of all cold dark matter (CDM) models of galaxy formation (e.g., Cole et al. 2000 and references therein). These currently favored models clearly predict that dark halos of modern galaxies were formed in the past through the process of repeated merging of, and buildup from, smaller systems. Although CDM models predict that dark halos merge, it is not clear whether galaxy formation or star formation occurs during, before, or after dark-halo mergers. If baryons collapse to form stars in dark halos before a significant amount of halo merging, then, based on dynamical friction arguments, we should witness mergers of galaxy stellar components. On the other hand, it is also possible that gas cools and forms stars after dark halos merge, producing the large galaxies we see today (e.g., Noguchi 2000).

One method of determining whether and how galaxies form by merging is to directly measure the fraction of galaxies undergoing mergers and mass assembly occurring by mergers at various look-back times, and estimate from these merger and mass assembly rates. While the star formation history of the universe is retrievable in part by examining nearby resolved galaxy stellar “fossil” populations, the mass assembly history for nearby galaxies is mostly lost through equilibrium and relaxation processes. Some merger tidal debris may remain for several gigayears, such as in our own galaxy (e.g., Ibata et al. 2002; Newberg et al. 2002), although these are likely the result of recent minor mergers. There is also considerable observational evidence for recent major mergers in the local universe (e.g., Schweizer &

<sup>1</sup> California Institute of Technology, Mail Code 105-24, Pasadena, CA 91125.

<sup>2</sup> National Science Foundation Astronomy and Astrophysics Postdoctoral Fellow.

<sup>3</sup> Department of Astronomy, University of Wisconsin, 475 North Charter Street, Madison, WI 53706-1582.

<sup>4</sup> Space Telescope Science Institute, 3700 San Martin Drive, Baltimore, MD 21218.

<sup>5</sup> Department of Astronomy, University of Arizona, Tucson, AZ 85721-0065.

Seitzer 1988; Borne et al. 2000) and accretion of low-mass galaxies onto larger ones (Zaritsky & Rix 1997). However, direct evidence for an increase in the galaxy merger rate at high redshift has not yet been established, despite the considerable circumstantial evidence. This includes evolving luminosity functions (e.g., Lilly et al. 1995; Ellis et al. 1996) and the appearance of distant “irregular” galaxies seen in *HST* WFPC2 images (e.g., Driver et al. 1998; Glazebrook et al. 1995; Abraham et al. 1996). Indeed, an enhanced past merger rate can plausibly explain the “faint blue galaxy” excess and may well be the physical mechanism driving the evolution of the blue galaxy luminosity function seen at intermediate redshifts. This idea was suggested over a decade ago (Broadhurst, Ellis, & Glazebrook 1992), but direct evidence for evolution in the galaxy merger rate has not yet been established.

The most popular method for measuring the evolution of galaxy mergers at high redshift is through pair counts (e.g., Zepf & Koo 1989; Burkey et al. 1994; Patton et al. 1997; Wu & Keel 1998; Le Fèvre et al. 2000) or kinematic pairs (Carlberg et al. 2000). After correcting for selection effects and biases (e.g., Patton et al. 2000), pair-count methods can be used to study major galaxy mergers out to  $z \sim 1$ . At high redshifts, however, this method becomes difficult and expensive in telescope time because of the many redshifts needed. There has, in fact, never been a measurement of merger fractions or merger rates at redshifts  $z > 1$ , although detections of high-redshift galaxy merging have been claimed (e.g., Neuschaefer et al. 1997).

Perhaps the best way to understand and characterize the merging process is to observe high-redshift galaxies and determine which are undergoing mergers based on their stellar light distributions. We argue in this paper and in Conselice (2003) that this can be done using the observed structures of galaxies. At high redshifts we can do this using the Hubble Deep Field (HDF) (Ferguson, Dickinson, & Williams 2000). Conselice et al. (2000a, hereafter CBJ00), Conselice et al. (2000b), and Conselice (2003) argue that galaxies undergoing major mergers can be identified through their large structural asymmetries, one aspect of the CAS (concentration, asymmetry, clumpiness) morphological system (Conselice 2003).

Previously, a color-asymmetry diagram was used by Conselice & Bershadsky (1999) to determine the fraction of galaxies undergoing mergers in the HDF, based on the original WFPC2 images, finding a merger fraction of 40%. These previous studies, however, are potentially biased by morphological  $K$ -corrections, where a galaxy’s appearance in the rest-frame UV is not necessarily similar to its rest-frame optical morphology. This problem is removed in this paper through the use of HDF NICMOS images, where the rest-frame optical light of galaxies is sampled out to  $z \sim 2.5$ .

By using the CAS system on galaxies found in the Hubble Deep Field North (Williams et al. 1996), and after understanding systematics and biases through simulations, we are able to measure the major merger history of galaxies out to  $z \sim 3$ . We use rest-frame  $B$ -band asymmetries with other structural and photometric indices, such as radii, absolute magnitude ( $M_B$ ), and stellar masses ( $M_*$ ), to further address the question of how galaxy mergers have evolved over time. Using this method, we find that out to  $z \sim 1$  the fraction of galaxies involved in major mergers increases, as has previously been noted (e.g., Le Fèvre et al. 2000; Patton et al. 2000). We argue that the fraction of galaxies under-

going mergers is lower for the fainter and lower mass galaxies at higher redshifts. The merger fraction does, however, continue to increase with redshift for the brightest and most massive systems. Based on this finding, we compute and quantitatively characterize the merger and mass assembly rates of galaxies due to merging out to  $z \sim 3$ . We also investigate how the fraction of the total stellar mass density in galaxies involved in major mergers changes with time, magnitude, and mass, and we compare our results with predicted values from cold dark matter models.

This paper is organized as follows: Section 2 is an explanation of the data, including redshift information and how the asymmetry parameter is measured for HDF galaxies. In § 3 we briefly explain the basis for our argument that structures of galaxies holds information from which a merger origin can be derived; § 4 gives the basic results of the asymmetry measurements and how they correlate with other physical properties, including absolute magnitude, color, and stellar mass, to argue that we can determine the merger history of galaxies out to  $z \sim 3$ . Section 4 further explores the comparison of merger histories with cold dark matter (CDM) models, and § 5 is a summary. The cosmology  $H_0 = 70 \text{ km s}^{-1} \text{ Mpc}^{-1}$ ,  $\Omega_m = 0.3$ , and  $\Omega_\lambda = 0.7$  is used throughout this paper.

## 2. PHOTOMETRIC DATA AND PARAMETERS

### 2.1. Imaging Data

The images we use for our morphological analyses were acquired with the *Hubble Space Telescope* as part of the Hubble Deep Field North optical and near-infrared campaigns. Optical data from the Wide Field Planetary Camera 2 (WFPC2) of the HDF-N (Williams et al. 1996) are combined with near-infrared (NIR) observations of the same field taken with the Near Infrared Camera and Multi-Object Spectrometer (NICMOS) (Dickinson 1998; Dickinson et al. 2000). The optical data consist of images in the WFPC2 filters: F300W ( $U$ ), F450W ( $B$ ), F606W ( $V$ ), and F814W ( $I$ ). The NICMOS HDF-N images were taken in 1998 June with observations in the F110W ( $J$ ) and F160W ( $H$ ) near-infrared bands. We also use a deep  $K$ -band image obtained with the Kitt Peak Mayall 4 m telescope.

From these images, a total of 1212 galaxies in the HDF were detected with SExtractor at AB magnitudes brighter than  $J = 27$ , based on the photometry of Dickinson et al. (2000). We compute magnitudes and radii (§ 2.3) for these galaxies within segmentation maps produced by SExtractor (Bertin & Arnouts 1996). These galaxies constitute the sample used throughout this paper, although we effectively use only a fraction of them, as we only consider galaxies with  $M_B < -18$  to avoid strong selection effects and biases (§ 2.3).

The shapes, sizes, structures, and morphologies of HDF galaxies, as observed in these six passbands, are affected by instrumental effects, such as point-spread functions, in addition to the intrinsic morphological  $K$ -corrections and surface brightness dimming. The angular resolution of the NICMOS HDF images is poorer than that of the WFPC2 data because of the longer wavelength diffraction limit and the pixel undersampling of NICMOS camera 3. The effective PSF FWHM is approximately  $0''.22$ . To minimize systematic errors associated with comparing galaxies at different resolutions (CBJ00), we have convolved the WFPC2

images to match the NICMOS PSF and made all morphological measurements from these PSF-matched data. Note also that the angular diameter distance to galaxies varies by less than 40% over the redshift range  $0.5 < z < 3$ , and by less than 20% for  $0.7 < z < 3$ , where the vast majority of the galaxies analyzed in this paper lie. Therefore, the resolution of our data in linear physical units (e.g., kiloparsecs) is nearly constant over the redshift and wavelength ranges considered here.

## 2.2. Redshifts, Photometry, and Stellar Masses

Photometry is done in all six HDF passbands and the  $K$ -band image for every galaxy, with photometric redshifts derived based on observed spectral energy distributions (Budavari et al. 2000). We use these photometric redshifts and spectroscopic ones, when available, to compute the rest-frame absolute  $B$ -band magnitude,  $M_B$ , and rest-frame Johnson  $B-V$  color for each galaxy. Rest-frame magnitudes and colors are computed by fitting the spectral energy distributions (SEDs) of each galaxy to templates. The best-fit template is then used to calculate the  $B-V$  color of each

galaxy based on interpolation of its observed SED. A total of 157 spectroscopic galaxy redshifts were available to us from Cohen et al. (2000), Dawson et al. (2001), and K. Adelberger & C. Steidel (2000, private communication). Figure 1 shows the absolute magnitude distribution of all galaxies to our magnitude limit of  $J = 27$ , with derived  $B-V$  colors, plotted as a function of redshift ( $z$ ).

The stellar masses used in this paper come from the analysis of Papovich et al. (2001), Papovich (2002), and Dickinson et al. (2003a, 2003b). The stellar masses are derived using the seven-band photometry described above and by assuming an initial mass function (IMF), metallicity, and a star formation history. The star formation history can be modeled, for example, as instantaneous, “bursty,” or exponentially declining. While there are several different possible IMFs and star formation histories for these galaxies, we use the model results of Papovich (2002), where the IMF is Salpeter, the metallicity solar, and the star formation history of each galaxy is monotonic. The stellar masses are also not computed for all the galaxies in the HDF, as many are too faint for a reliable computation.

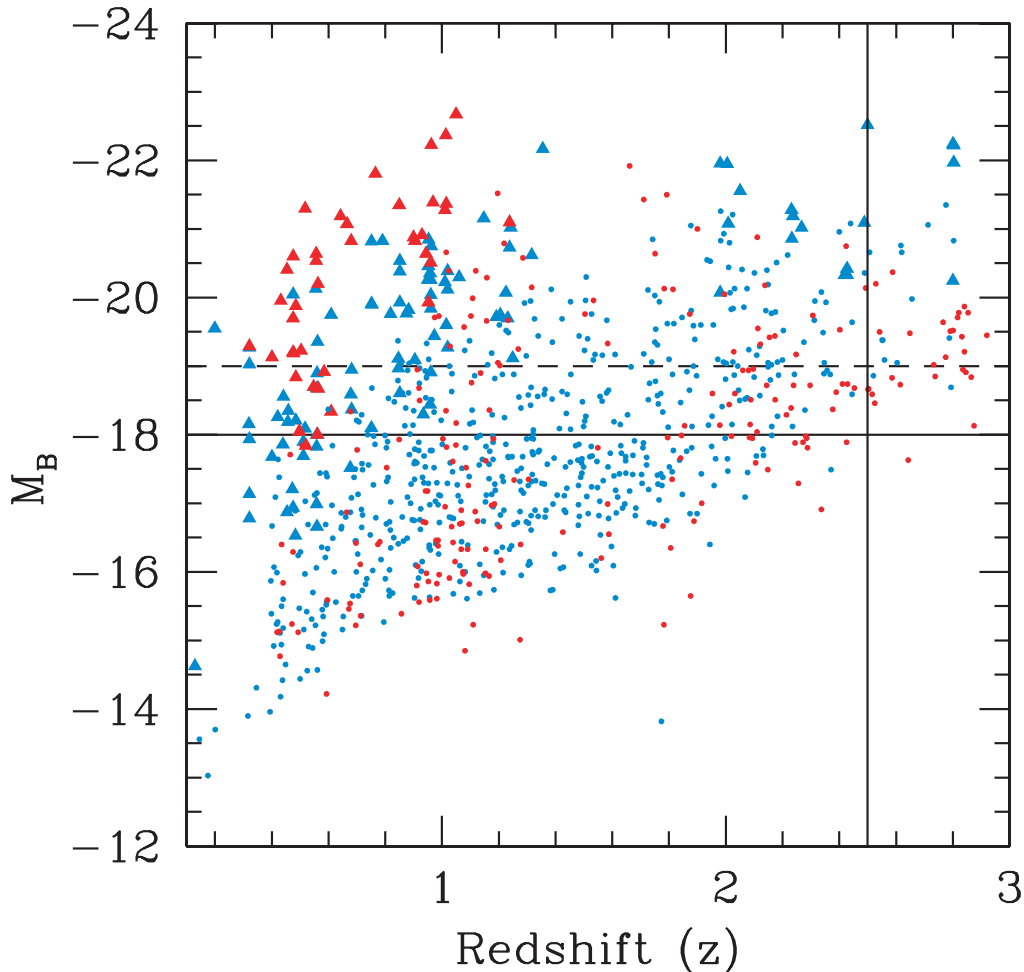


FIG. 1.—Plot of absolute magnitude vs. redshift for galaxies in the Hubble Deep Field North. The red symbols are for objects with  $(B-V)_{\text{rest}} > 0.5$  and blue symbols are for  $(B-V)_{\text{rest}} < 0.5$ . The large symbols are objects with confirmed spectroscopic redshifts, while the smaller symbols are those objects with photometric redshifts. The vertical line at  $z \sim 2.5$  is the limit we use for obtaining reliable morphological parameters and galaxy detections, and the solid and dashed horizontal lines show the  $M_B < -18$  and  $M_B < -19$  lower luminosity limits we use throughout this paper (see text).

For this particular choice of IMF, metallicity, and star formation history the typical uncertainties on the stellar masses are about a factor of 2 (Papovich et al. 2001; Papovich 2002). The uncertainties are larger at higher redshifts, where the photometric data do not reach red rest-frame wavelengths, and for the bluest galaxies, where varying amounts of stellar mass can be hidden by the bright light of ongoing star formation.

### 2.3. Asymmetries

#### 2.3.1. Computing Asymmetries

The main quantitative structural parameter used in this paper is the asymmetry ( $A$ ) index, one property of the CAS physical morphology system (Conselice 2003). Asymmetry has been used previously as a morphological parameter for nearby (Conselice 1997; CBJ00) and distant galaxies (e.g., Shade et al. 1995; Abraham et al. 1996; Conselice & Bershadsky 1999). The asymmetry computation we use is described in detail in CBJ00. The basic computation of  $A$  involves rotating and subtracting a galaxy image from itself and comparing the summation of the absolute value of these residuals to the original galaxy's flux.

Our computation differs from the prescription set out in CBJ00 through our use of the SExtractor dimensionless, "Kron radius multiplier" ( $k_r$ ), times a factor of the semi-major axis ( $a$ ), to define the area within which asymmetries are computed. The SExtractor Kron radius multiplier is a dimensionless quantity used to scale the ellipse whose semi-major ( $a$ ) and semiminor ( $b$ ) axes are defined by first moments of the light profile. This is different from the prescription of CBJ00 where the Petrosian (1976)  $\eta$  radius was used. However, comparisons of the  $\eta$  radius used in CBJ00 and the first moment radii for bright HDF galaxies reveals that the maximum difference of  $k_r \times a$  (hereafter Kron radius) and the Petrosian radius is very small, usually a few pixels ( $\sim 0''.5$ ) at most, and always different by less than 10%. Asymmetries computed using the two methods are also indistinguishable for galaxies in the HDF. Simulations also show that defining the radius in this manner is robust when a galaxy is moved to higher redshifts (§ 2.3.5).

Asymmetries are computed for all galaxies in each observed WFPC2 and NICMOS band. The rest-frame  $B$ -band asymmetries are then derived using the spectroscopic or photometric redshift of each galaxy, and then interpolating rest-frame  $B$ -band asymmetries using the observed asymmetries. The rest-frame  $B$ -band asymmetry is computed in this way through a linear combination of the asymmetry values in the two filters nearest the rest-frame  $B$ -band wavelength. For galaxies at  $z > 2.6$ , where the central rest-frame  $B$ -band filter wavelength becomes higher than the central wavelength of the  $H$  band, we assume  $A(B)_{(\text{rest})} = A(H)_{(\text{Obs})}$ .

There are, however, many biases and random and systematic errors that must be understood in detail and accounted for before we can reliably interpret and use these asymmetry values to derive evolution. The general procedure for measuring asymmetries, as outlined above, relies on a robustly defined center, radius, and background area. As the Hubble Deep Field North is crowded with galaxies, but not confusion limited, finding suitable background areas to measure sky statistics is not trivial. We examine this problem and the centering and radius issues later in this paper, although see CBJ00 for a detailed description of these problems using

nearby galaxies. To address some of these issues, we examine a subsample of the 38 brightest HDF galaxies, with  $M_B < -18$ , at redshifts  $0.4 < z < 0.7$  in the HDF to determine how centering routines, differing radii and background subtraction methods affect the measured asymmetries. We also measure asymmetries within radii defined within the SExtractor region, and we investigate possible galaxy contamination in § 3.3.

#### 2.3.2. Asymmetry Systematics with Radius

The problem with choosing a radius to measure asymmetries, as well as other structural parameters, lies in the trade-off between galaxy coverage and noise, including contamination from other galaxies. CBJ00 determined that the larger the radius, the more representative the computed asymmetry index is in comparison with a fiducial "total" asymmetry, and the better its asymmetry values correlate with other physical properties. On the other hand, if radii used for computing asymmetries are large, then more background will be present in the computation, which increases the noise on the asymmetry measurement. A larger radius also increases the chance of contamination from other galaxies and thus requires careful attention to neighboring objects.

While there is no foolproof way of determining the best radius to measure asymmetries, we can constrain this to some extent by examining asymmetries of the relatively nearby galaxy sample in the HDF computed at various factors of the Kron radii. These measurements are plotted in Figure 2 as a function of the Kron radii as measured by SExtractor. The asymmetry parameter is measured for the 38 nearby galaxies in the HDF at five different radii:  $0.25 k_r \times a$ ,  $0.5 k_r \times a$ ,  $1.0 k_r \times a$ ,  $1.5 k_r \times a$ , and  $2.0 k_r \times a$ . The average and  $\pm 1 \sigma$  variations of the asymmetries for these

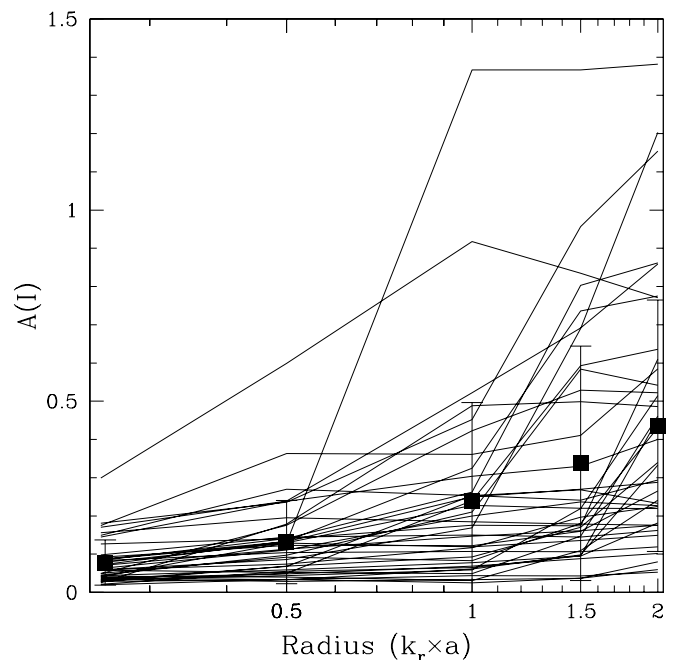


FIG. 2.—Plot of the asymmetries computed in the  $I$  band for the 38 galaxies in the HDF with  $M_B < -18$  and at  $0.4 < z < 0.7$  at various fractions of the Kron multiplier ( $k_r$ ) times semimajor axis ( $a$ ) radii. The solid box is the average asymmetry value at every radius, while error bars represent the  $1 \sigma$  variation of these averages.

38 galaxies at these radii are  $0.08 \pm 0.06$ ,  $0.13 \pm 0.11$ ,  $0.24 \pm 0.26$ ,  $0.34 \pm 0.31$ , and  $0.44 \pm 0.33$ .

As for nearby galaxies (e.g., CBJ00), asymmetries increase at higher radii. Some of the higher asymmetries at larger radii are the result of contamination from nearby galaxies. We also find that errors on individual asymmetry measurements increase when using larger measuring radii. To strike a balance between representative radius and noise on individual measurements, we use the radii  $0.5 \times k_r \times a$  to measure asymmetries. This is also the radius that matches the apparent radius when estimated by eye. Through tests we found this radius to be similar to the  $r(\eta = 0.2)$  radius used to measure asymmetries for nearby galaxies, and these radii can be robustly measured for galaxies out to redshifts of  $z \sim 3$  (§ 2.3.5).

### 2.3.3. Search Radii

CBJ00 found that asymmetries do not significantly depend upon the search size used to find the minimum asymmetry. The search size is the pixel size that the asymmetry computation code uses to find the minimum asymmetry by computing  $A$ -values at centers that differ by the search size (CBJ00) until the minimum asymmetry is found. We tested this on the HDF data using several different search radii and always found the same asymmetry, independent of search size. For example, when changing the search radius from 0.5 to 0.1 pixels, the values of the asymmetries only change by  $\delta A = 0.04$  at most.

### 2.3.4. Background Measurement Systematics and Effects of Correlated Noise

The method of background removal is a very important issue, which we address here in some detail. The asymmetry computation as outlined in § 2.3.1 needs to be corrected for background noise, and this is usually done using a patch of sky in the image that contains no part of any galaxy. This approach is necessary as an annulus surrounding a galaxy may be contaminated by faint outer regions that have dimmed below the noise level (e.g., the Tolman effect; Tolman 1930).

The background noise level in our images varies from place to place in the NICMOS images and to a lesser extent the WFPC2 data, as a result of variations in quantum efficiency and dark current noise over the detector array. For this reason, no one “blank spot” used to constrain background noise in the asymmetry measurements can be considered wholly representative. To determine the degree to which this may affect the asymmetries, we show in Figure 3 the asymmetries of all the 1212 galaxies measured using five different background regions throughout the HDF images (listed as asymmetry runs 1 through 5). These five background regions are at the same physical place in each band and were carefully chosen to span the area of the HDF. We only show the resulting asymmetry distributions in Figure 3 for the  $I$ - and  $H$ -band asymmetries, but these are representative of the  $B$ -,  $V$ -, and  $J$ -band asymmetries, respectively.

As can be seen, the  $I$ -band asymmetries are relatively constant using the different backgrounds, but the  $H$ -band asymmetries can and do vary. To overcome this problem, the effective asymmetry measured in each band is found by averaging the asymmetries for the five different backgrounds. The  $1 \sigma$  variation in these measurements is added

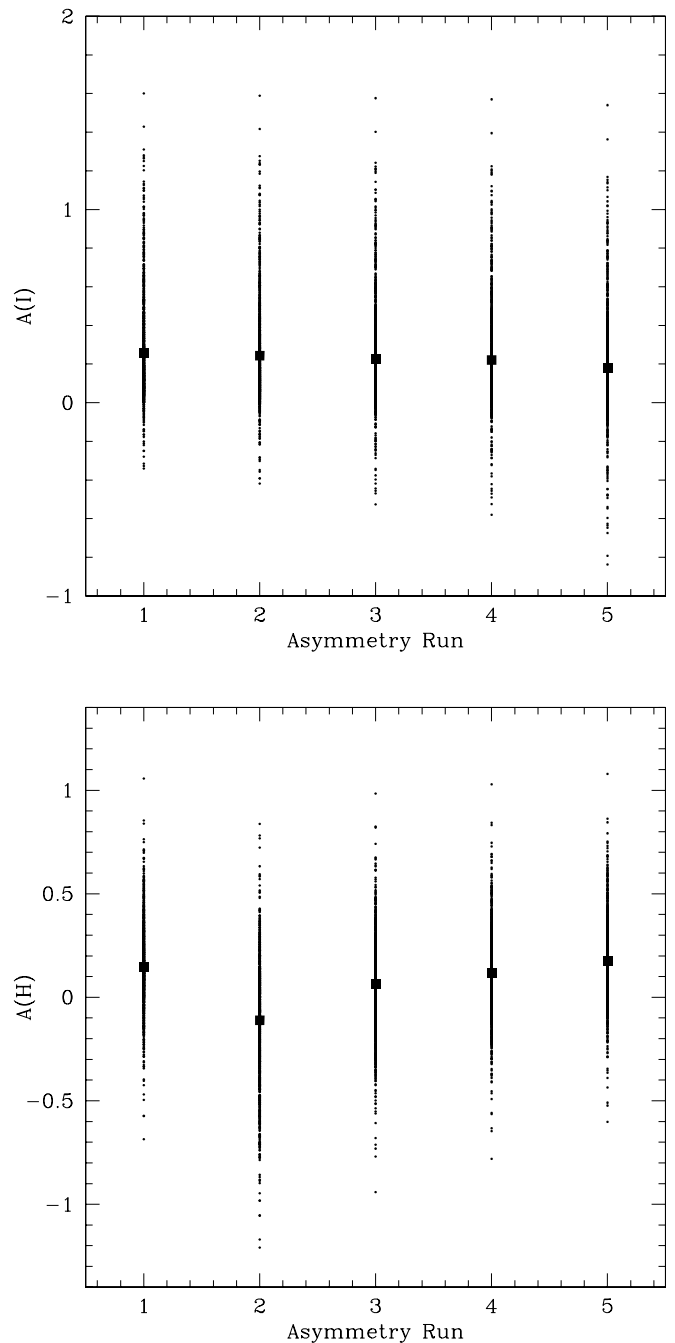


FIG. 3.—Distribution of asymmetries for all 1212 galaxies observed in the HDF as measured in the F814W ( $I$ ) band and the F160W ( $H$ ) band after using five different background positions for computing the background correction.

in quadrature to the average asymmetry measurement error, and this value is used as the asymmetry error.

We also performed a series of simulations to determine the effects of correlated noise on the measurement of asymmetries. This was done by creating fake noise maps and placing galaxies into them and then measuring their asymmetries. When we correlate the noise by smoothing the initial noise map by some filter and then remeasure the resulting asymmetries, we find that the variation in  $A$  is tiny,  $\delta A \sim \pm 0.03$ . This is due to the fact that we empirically remove the background by using a patch of sky, which in

principle matches the noise pattern under the galaxy being studied.

### 2.3.5. Detection and Simulations of Asymmetry Variations with Redshift

A significant issue that must be addressed in any study that compares properties of galaxies at different redshifts is the fact that measured properties, as well as the detection of galaxies themselves, change solely as a result of redshift effects. The rapidly increasing luminosity distance of galaxies, with the slowly changing angular size distance, produces a  $(1+z)^4$  decline in surface brightness. The result is that objects we detect in the HDF at lower redshifts might not be detectable at higher redshifts, thereby invalidating some comparisons. Changes in the signal-to-noise ratio (S/N) and resolution due to redshift can also mask, or mimic, real evolution. We address these issues using simulations and apply this information to correct our asymmetry measurements and to understand our detection completeness. Note that we always use interpolated rest-frame  $B$ -band values of each galaxy; thus, we remove all morphological  $K$ -corrections.

Simulations were carried out by using the 38 galaxies at  $0.4 < z < 0.7$ , which have  $M_B < -18$ , as described in § 2.3.1. The images of these objects in their approximate rest-frame  $B$  band (observed F606W, or  $V$  band) are simulated as they would appear at various redshifts from  $z = 1$  to 3 in the redder HDF filters (at  $z > 3$  we can no longer sample rest-frame  $B$  morphologies). These simulations were done by creating the background for each of the HDF bands with the same noise characteristics, then randomly placing the simulated galaxies into these backgrounds. The galaxies are reduced in resolution, signal to noise, flux, and surface brightness, and convolved with either the NICMOS or WFPC2 PSF (see Conselice 2003).

After these galaxies were simulated, we ran the SExtractor detection software using the exact same criteria used for the original HDF detections (Dickinson et al. 2003b). From this we are able to determine the detection completeness at each simulated redshift and measure the asymmetries and radii of the galaxies detected. Doing this allows us to better understand the systematics produced by nondetections and how asymmetry changes because of cosmological effects, as opposed to real evolution. We

TABLE 1  
SIMULATION RESULTS

Redshift ( $z$ )	Number Detected (%)	$\delta(A)^a$	$\delta(r)^a$ (arcsec)
0.5.....	38 (1.00)	0	0
1.0.....	38 (1.00)	$0.05 \pm 0.09$	$0.12 \pm 0.14$
1.5.....	38 (1.00)	$0.04 \pm 0.07$	$0.11 \pm 0.10$
2.0.....	38 (1.00)	$0.04 \pm 0.08$	$0.14 \pm 0.14$
2.5.....	38 (1.00)	$0.06 \pm 0.09$	$0.20 \pm 0.17$
3.0.....	34 (0.89)	$0.06 \pm 0.12$	$0.26 \pm 0.27$
4.0.....	23 (0.61)	$0.08 \pm 0.13$	$0.41 \pm 0.45$
5.0.....	12 (0.32)	$0.11 \pm 0.16$	$0.62 \pm 0.68$

<sup>a</sup>  $\delta(A)$  and  $\delta(r)$  are the differences between the originally measured asymmetries and radii for the 38 galaxies at  $0.4 < z < 0.7$  simulated at higher  $z$  and the resulting values measured when the galaxy is at the given higher redshift ( $z$ ).

simulate this local sample of HDF galaxies to redshifts  $z = 1, 1.5, 2, 2.5, 3, 4, 5$ , and 6. While we do not discuss real HDF galaxy asymmetries for objects above  $z \sim 3$  in this paper, we include these higher redshift simulations for completeness and to investigate trends with redshift.

The results for these simulations are shown in Figure 4 and are quantified in Table 1. First, all of the 38 objects we simulate from low  $z$  remain detectable until  $z \sim 2.5$ , when the completeness begins to drop (Fig. 4). The measured values of the asymmetries generally become lower at higher redshifts (Fig. 4). The average corrections necessary to account for these effects are listed in Table 1 and are generally low, with differences  $\delta A = 0.04$ – $0.06$  for the redshift ranges studied in this paper.

There is also only a very slight difference in retrieved asymmetries for faint galaxies with different magnitudes in each redshift range. The fainter galaxies at each redshift range are generally affected by noise more, and hence the systematics effects (and corrections) are larger, with values  $\sim 0.02$  higher, on average, than the brighter systems. As this is usually smaller than the random measurement errors for these faint galaxies, we do not account for this small difference. As discussed in CBJ00, where similar simulations are done in terms of S/N and resolution, the asymmetry index is not greatly affected by the reduced resolution and lower S/N for galaxies with  $M_B < -18$ . Figure 4 does show,

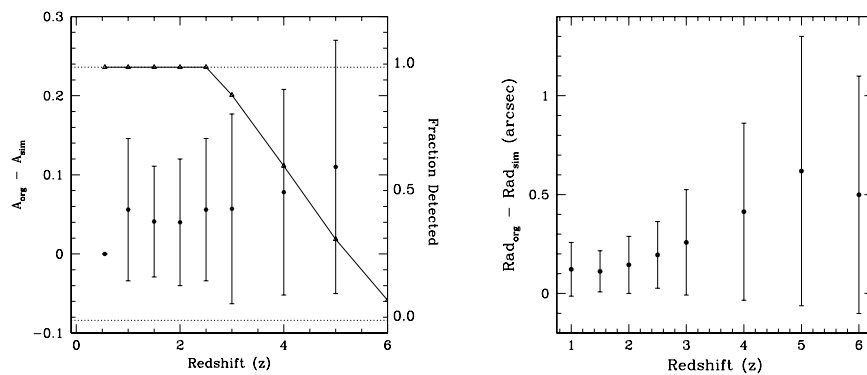


FIG. 4.—Results of simulating the 38 HDF galaxies at  $0.4 < z < 0.7$  and  $M_B < -18$  to higher redshifts and then redoing the entire asymmetry analysis from detection to measurement. The left panel shows the average and  $1\sigma$  variation of the asymmetry difference between the original asymmetry and the simulated asymmetry ( $A_{\text{org}} - A_{\text{sim}}$ ). Also plotted on the right side of the left panel is the fraction of the 38 galaxies that are detected through SExtractor after performing the simulation. The right panel shows the average and  $1\sigma$  variations of the difference (in arcseconds) between the original radii measured ( $\text{Rad}_{\text{org}}$ ) and the simulated radii ( $\text{Rad}_{\text{sim}}$ ).

TABLE 2  
AVERAGE RANDOM ASYMMETRY ERRORS AT VARIOUS MAGNITUDE AND REDSHIFT LIMITS

Redshift Range	$-19 < M_B < -18$	$-20 < M_B < -19$	$-21 < M_B < -20$	$M_B < -21$
0–1.0 .....	0.02	0.01	0.01	0.00
1–2.0 .....	0.14	0.07	0.04	0.03
2–3.0 .....	0.18	0.13	0.08	0.04
3–3.5 .....	0.19	0.17	0.15	0.10

however, that, by using a magnitude limit of  $M_B = -18$ , we begin to become incomplete at redshifts  $z > 2.5$ .

Our radii, defined as  $0.5 \times k_r \times a$  (§ 2.3.1), also shows a slight decrease when the 38 low-redshift galaxies are simulated to higher redshift and then redetected with SExtractor (Fig. 4, *right*). For the remainder of the paper we use these results to apply slight corrections (Table 1) to the measured asymmetries and radii for galaxies found in the HDF at  $z > 0.7$ .

### 2.3.6. Final Asymmetry Values and Errors

The final asymmetry for each galaxy in every band is computed by taking the average of the asymmetry values computed using the different backgrounds (§ 2.3.4) and, depending on the redshift, applying a systematic error correction as described in § 2.3.5. The error of each asymmetry measurement is computed by combining the average measured error with the rms of the asymmetry values. The average errors on our asymmetry values remain extremely low for the brightest galaxies at  $M_B < -21$  with  $\langle \delta A \rangle = 0.04$  out to  $z \sim 3$  (Table 2). All of the random errors in fact remain rather low, except for the faintest galaxies with  $M_B > -19$ , at  $z > 2.5$ , where the errors approach  $\langle \delta A \rangle \sim 0.2$ .

The rms variations of computed  $A$ -values using different sky patches is almost always lower than the computed random errors for each asymmetry measurement. The average

random asymmetry errors are plotted as a function of redshift and magnitude in Figure 5 as solid lines, and they are listed in Table 2. The final corrected asymmetries values are plotted as a function of redshift in Figure 5.

## 3. METHODOLOGY

### 3.1. The Merger Criterion

A major goal in contemporary astrophysics is determining how galaxies formed and evolved. As we approach this goal, it is fair to ask if the structures of galaxies give any clues toward solving this problem. Is it possible that the morphological appearance of a galaxy is only representative of temporary “weather” and does not relate to the fundamental underlying evolution? While we only briefly address these questions here, see Conselice (2003) for a detailed discussion and an introduction to the CAS (concentration, asymmetry, clumpiness) classification system, where it is quantitatively argued that galaxy structures reveal fundamental information.

In general, a galaxy’s appearance or morphology is determined by a variety of different effects. Some of these are produced by projection, most notably in the case of edge-on spiral galaxies, but, as argued in Conselice (2003), morphology is largely the result of physical processes, such as star formation and interactions and mergers with other galaxies, and the past history of these events.

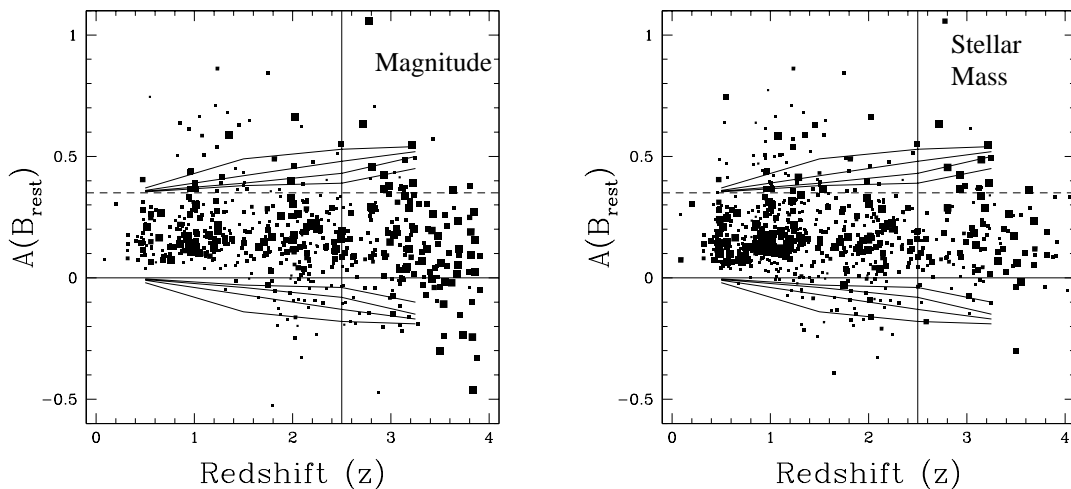


FIG. 5.—Plot of the rest frame  $B$ -band asymmetry measurements  $A(B_{\text{rest}})$  as a function of redshift ( $z$ ). The size of the plotted point is proportional to (*left*) the luminosity (magnitude) of the galaxy and (*right*) the stellar mass of the galaxy. The smallest points are objects with (1)  $-18 > M_B > -19$ , (2)  $8 < \log M_* < 9$ . The larger symbols are for galaxies with (1)  $-19 > M_B > -20$ , (2)  $9 < \log M_* < 9.5$ , and (1)  $-20 > M_B > -21$ , (2)  $9.5 < \log M_* < 10$ . The largest symbols are for galaxies with (1)  $-21 > M_B > -23$  and (2)  $\log M_* > 10$ . The solid line is  $A(B_{\text{rest}}) = 0$  and the dashed line is the limit for mergers at  $A(B_{\text{merger}}) = 0.35$ . The solid diagonal lines originating at  $A(B_{\text{rest}}) = 0$  and  $A(B_{\text{merger}}) = 0.35$  show the average random error on the asymmetry index as a function of redshift and limiting magnitude, such that each line is either  $A(z) = 0.35 + \text{error}(z)$  or  $A(z) = 0 - \text{error}(z)$ . These lines are for galaxies at magnitudes, from the nearest to their respective horizontal line outward,  $M_B < -21$ ,  $-21 < M_B < -20$ ,  $-20 < M_B < -19$ , and  $-19 < M_B < -18$ .

As described in CBJ00 and Bershady, Jangren, & Conselice (2000), using a computationally consistent method to compute asymmetries reveals strong and physically meaningful relationships with other parameters, such as color and concentration (CBJ00). This requires using a method for computing asymmetries that is not affected by choice of center, radius, or to first order, resolution.

To determine how useful asymmetry and other parameters are for distinguishing galaxies in various phases of evolution, CBJ00, Conselice et al. (2000b), and Conselice (2003) computed asymmetries for over 200 nearby galaxies in all phases of evolution, including high- $z$  analogs, such as starbursts and ULIRGs. When asymmetries are combined with color or other structural information, galaxy types, such as elliptical, spiral, and irregular galaxies, can be roughly distinguished from each other. As expected, ellipticals are symmetric, red objects; while later types are both bluer and more asymmetric (CBJ00). We also argue in these papers that galaxies undergoing major mergers can be distinguished from those evolving quiescently through their global asymmetries.

There are also fairly strong correlations between  $B-V$  colors and clumpiness ( $S$ ) values with the asymmetry index for nonmergers, such that more asymmetric galaxies are bluer and have higher clumpiness values. For these nonmergers there exists a small distribution of  $A$ -values at all  $S$  and  $B-V$ -values, with a natural scatter  $\sigma(A)$  in asymmetries (see Figs. 7 and 8 in Conselice 2003). We define these distributions in Conselice (2003) and use them to identify statistical outliers with high asymmetries, which we identify as mergers. If we set a limit of  $A_{\text{merger}} > A(S, B-V) + 3\sigma(A)$  for major mergers, then we find  $A(B)_{\text{merger}} \sim 0.35$  for both the bluest and most clumpy galaxies yet observed. Redder or less clumpy galaxies have a  $3\sigma(A)$  deviation less than  $A = 0.35$ ; thus, we are being conservative with this limit. From a nearby sample of  $\sim 240$  galaxies, nearly all objects that deviate more than  $3\sigma(A)$  from the asymmetry-color and asymmetry-clumpiness relationships (Conselice 2003) are galaxies involved in major mergers. As such, we use  $A(B)_{\text{merger}} = 0.35$  as our limit for identifying major mergers.

Other evidence that  $A(B)_{\text{merger}} > 0.35$  includes galaxies with asymmetries larger than  $A(B)_{\text{merger}}$  showing kinematic evidence for merging based on broadened H I line profiles (Conselice et al. 2000b). The measured asymmetries of simulated galaxies in major merger simulations also have  $A > 0.35$  when undergoing merging (Conselice & Mihos 2003). These simulated galaxies have lower asymmetries, with  $A < A(B)_{\text{merger}}$  before and after merging events.

### 3.2. Eddington Bias

We argue in § 4 that galaxies at higher redshifts are more asymmetric in their rest-frame  $B$ -band morphologies. We use this to further argue that, at the very least, the most massive galaxies must be forming through the merger process. An important question to ask, however, is how this result is biased by our observational random errors, which in noisy data can mimic higher merger fractions, analogous to the aberration in star or galaxy counts due to random errors (Eddington 1913).

The basic idea behind the Eddington bias is that, within an intrinsic distribution of some observed quantity, in the presence of more and more noise, there will be larger measurement tails. In star counts the effect is to scatter more

counts into bright bins from fainter bins. In this section we investigate if the increase in  $A$ -values can be explained by increased noise scattering intrinsically low asymmetry values into the high-asymmetry bins.

To investigate the importance of Eddington bias in producing higher measured asymmetries for galaxies at higher redshifts, we plot in Figure 6 the asymmetry values for our sample divided into different redshift and absolute magnitudes. We also list in Table 2 the average random error of the asymmetry values for the galaxies plotted in each of the redshift/absolute-magnitude bins shown in Figure 6. From these values and the other information in Figure 6, we argue that the Eddington bias is not a major effect when comparing asymmetries for galaxies at similar absolute magnitudes at different redshifts. The errors remain below  $\delta A = 0.10$  up until  $z = 3$  when they become large.

To show this and to understand the limitations of our data and the effects of random errors, we carry out Monte Carlo simulations, the results of which are plotted in Figure 6 as the number in the lower right of each panel. This number is the likelihood that an increase in claimed asymmetries between two bins is not due to an increase in random errors at higher redshifts. That is, it is the significance that any increase in asymmetries is real, and not due to Eddington bias.

These simulations are done by assuming that the random errors are Gaussian distributed, with a full width at half maximum given by the increase in the error listed in Table 2. To determine how significant our observed increase in asymmetries are at a given magnitude, we add in resulting random errors to the asymmetries for galaxies in the lowest redshift bin ( $0 < z < 1$ ). We then recompute the mean and standard deviation of the resulting asymmetry distribution. This allows us to determine the likelihood that an increase in average asymmetries and  $1\sigma$  distributions at different redshifts are due to an increase in random errors induced by being at higher redshifts.

The result of these simulations is that, in almost all cases, the statistical probability of a claimed asymmetry increase being due to a random configuration of increased errors is very small. Note that we do not claim an increase between each redshift interval for every magnitude (see § 4.4). From these simulations we are confident at the  $3-10\sigma$  level that all claims for increases in asymmetries between different redshifts is a real effect, and not a result of Eddington bias. The only exception is the change in asymmetries seen for the  $-20 > M_B > -21$  galaxies between  $0 < z < 1$  and  $1 < z < 2$ . This is the *only* interval in which a claimed increase in asymmetries has a significant less than  $3\sigma$ .

Note that we do not use the  $z > 3$  bin in our analysis and only show it here for comparison purposes. We latter quantify the Eddington bias in another way by always plotting the plus-or-minus random error merger fractions. Doing this, we find that the trend of increasing asymmetries at higher redshifts is still present, verifying the statistical argument made in this section.

### 3.3. Contamination from Projection

One potential problem with the asymmetry methodology is that occasionally two galaxies will overlap to produce a two-dimensional image that looks asymmetric. The two galaxies themselves can look very smooth and symmetric, but when projected on or near each other

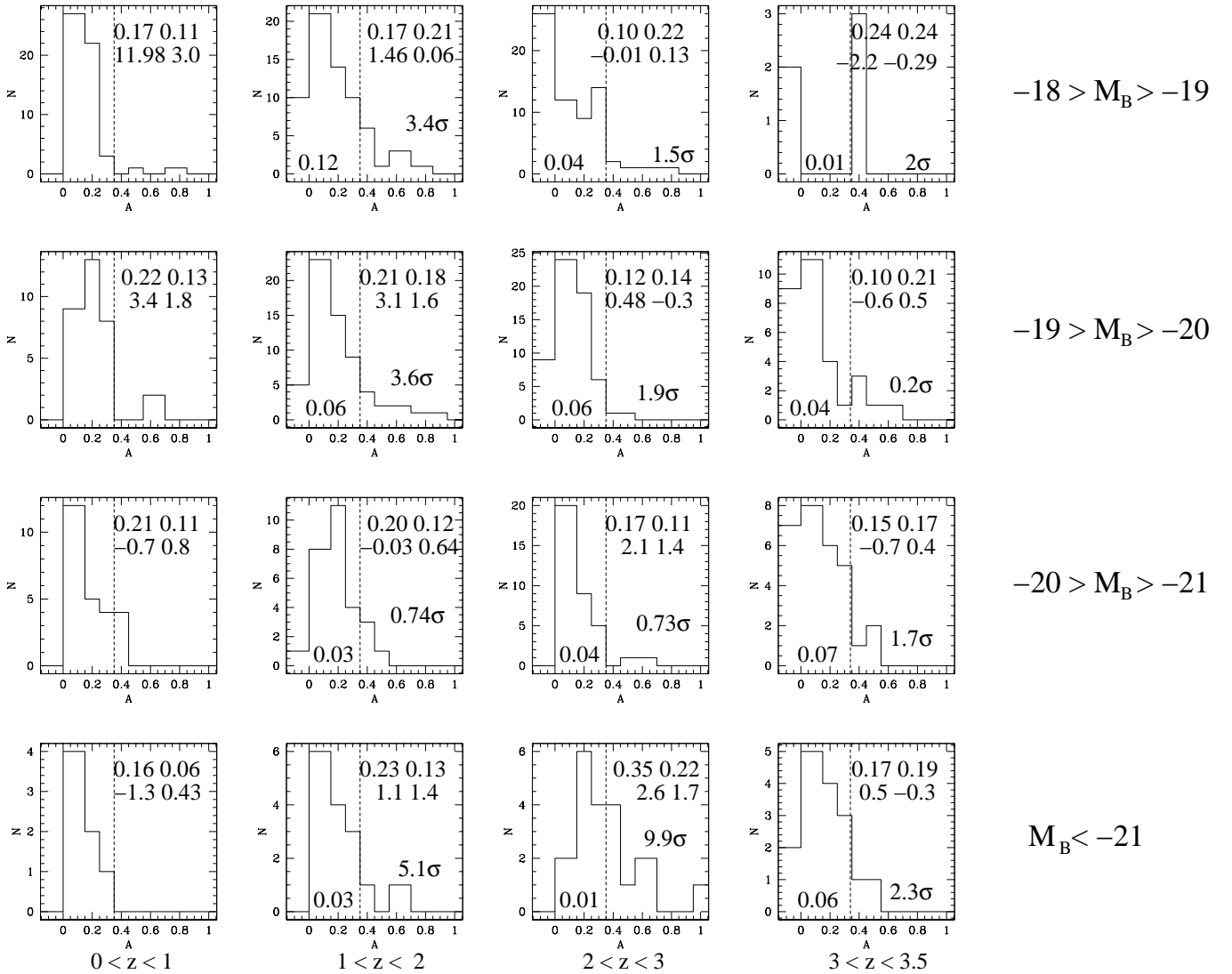


FIG. 6.—Distribution of asymmetries as a function of absolute magnitude and redshift. The top four numbers are (clockwise from top left) the mean asymmetry, its  $1\sigma$  variation, its skewness, and kurtosis values. The bottom left number is the difference in the average random error for the galaxies in that particular magnitude and redshift bin and the previous lower redshift bin at the same magnitude. The bottom right number is the significance, based on Monte Carlo simulations discussed in § 3.2, that an increase in asymmetries are not due to an increase in random errors. The dashed vertical line shows the  $A_{\text{merger}}$  limit.

they could potentially be identified as a major merger through a resulting high asymmetry. Although we only measure asymmetries for galaxies within well-defined radii produced through SExtractor, which deblends objects, there are still possible cases of near neighbors that could produce a higher signal.

As such, we must be able to constrain the importance of this effect. Overlapping galaxies in the Hubble Deep Field are rare, however, with only a handful of obvious cases (White, Keel, & Conselice 2000). Through a visual examination of all objects identified as a merger through asymmetries, only seven are galaxies that might be in pairs (Fig. 7). We say “might” here, as it is often the case that these pairs are real physical associations and some of the photometric redshifts suggest that they are in fact two nearby galaxies, perhaps in the early phases of a major merger. In any case, since our sample contains  $\sim 70$  galaxies identified as mergers, only 10% of our mergers have something that could resemble a pair, although many of these

show evidence of being real physical units in terms of similar colors and in at least one case similar spectroscopic redshifts, and thus are not chance projections.

## 4. RESULTS

### 4.1. Merger Candidates in the Hubble Deep Field

All galaxies brighter than  $M_B = -20$  between  $0 < z < 3$  found in the HDF are shown in Figure 7 in the F814W band, divided by redshift intervals:  $0 < z < 1$ ,  $1 < z < 2$ , and  $2 < z < 3$ . The mergers brighter than  $M_B = -20$  are also listed in Table 3. The images shown in Figure 7 are the appearance of each galaxy in F814W, with three numbers overplotted (top to bottom): absolute magnitude, rest-frame  $B$ -band asymmetry  $[A(B)_{\text{rest}}]$ , and redshift. Galaxies that are statistically likely to be merger candidates, with  $A(B) > 0.35$ , have a solid box in the upper right corner of their panel.

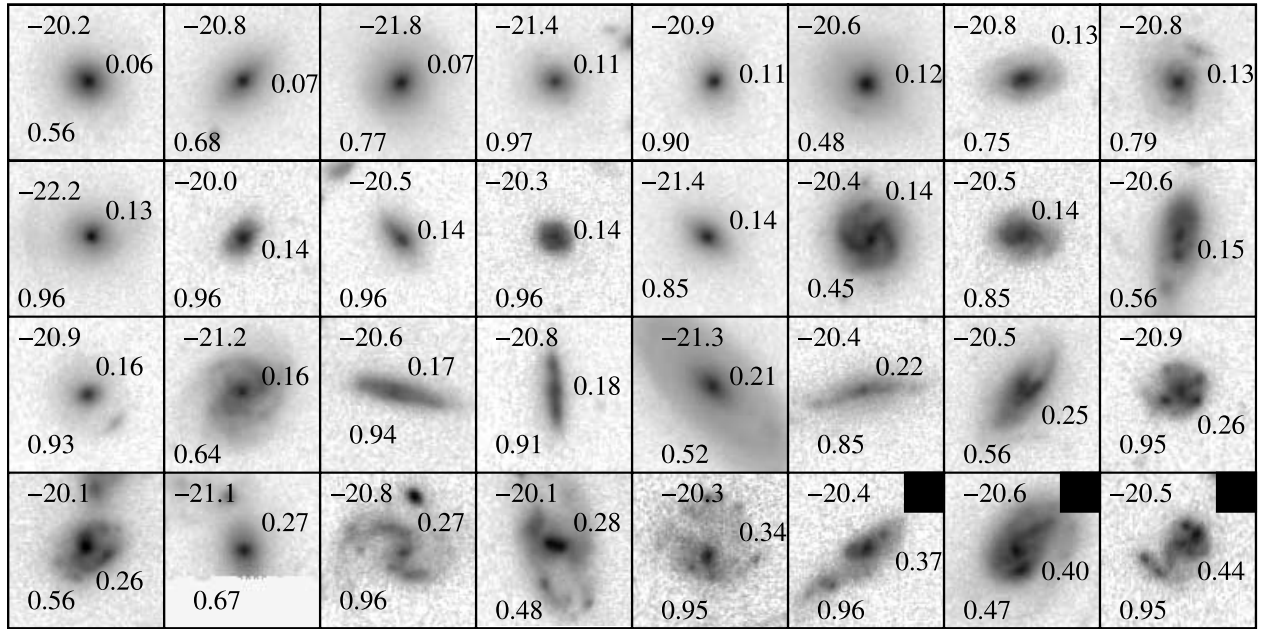


FIG. 7a

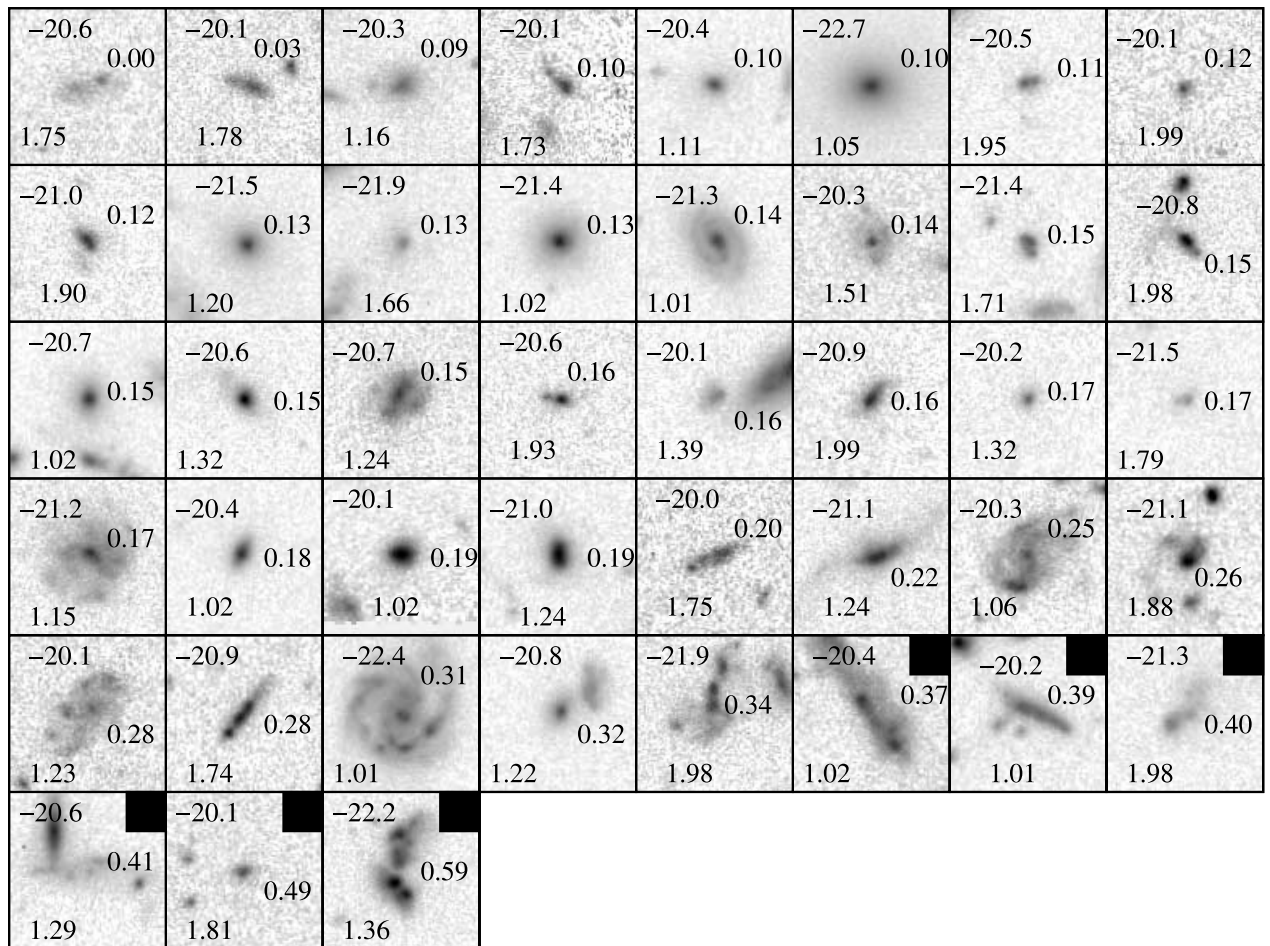


FIG. 7b

FIG. 7.—(a) Images of all galaxies in the Hubble Deep Field North with  $M_B < -20$ , between  $0 < z < 1$ , ordered by increasing asymmetry, as seen in the images F814W<sub>rest</sub>. The upper number in each panel is the  $M_B$  of each galaxy and the bottom number is its redshift, while the number on the right-hand side is the galaxy's  $A(B_{\text{rest}})$  value. Galaxies consistent with being mergers based on their asymmetries have a solid dark box in the right-hand corner of their respective panels. (b) Same as (a), expect all galaxies with  $M_B < -20$ , between  $1 < z < 2$  are shown. (c) Same as part (a), expect all galaxies with  $M_B < -20$ , between  $2 < z < 3$  are shown.

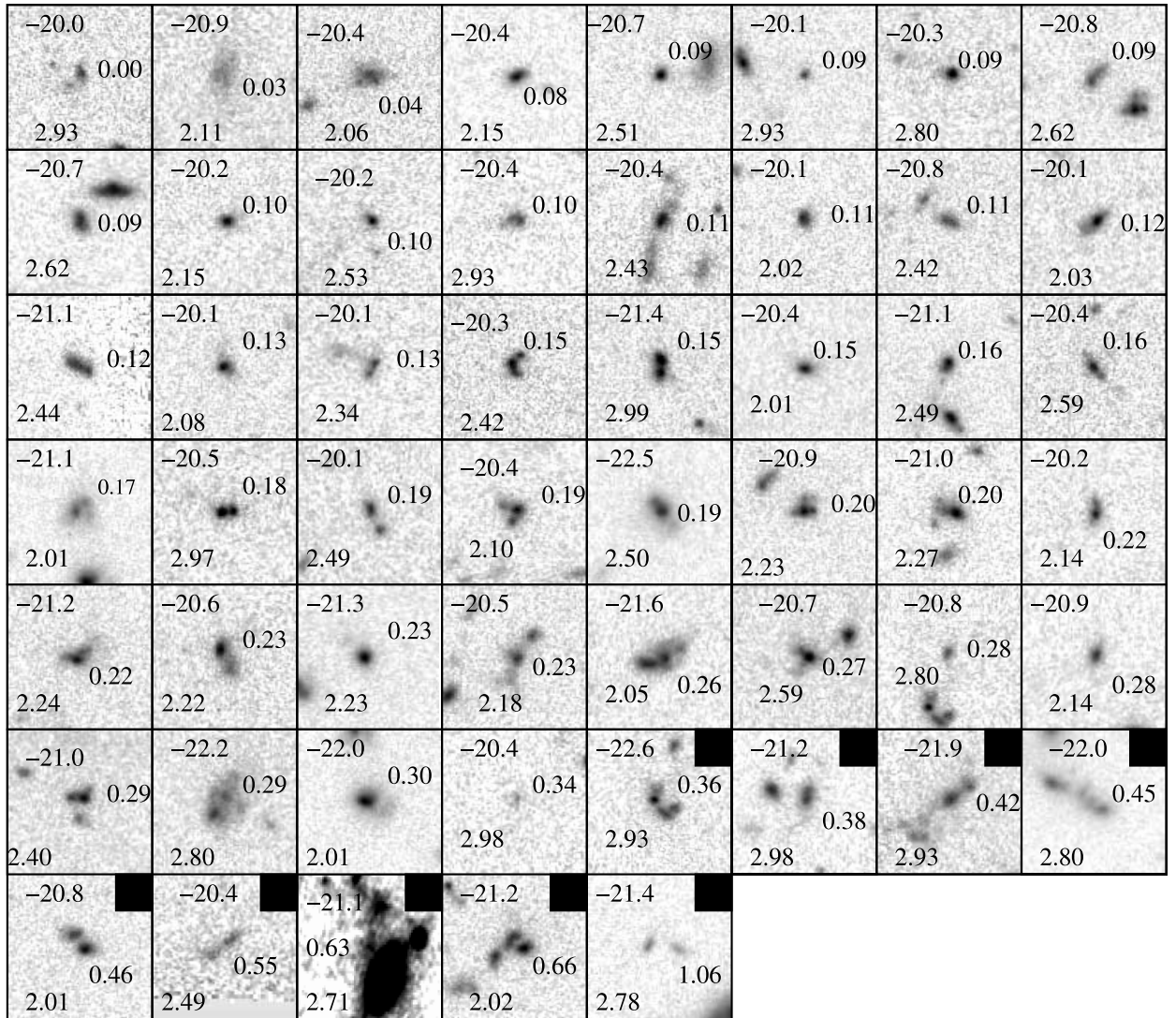


FIG. 7c

This figure shows, among other things, that the asymmetry index is able to pick out systems that would be chosen as mergers through visual estimates. Systems with high asymmetries, however, are clearly in various phases of merging. Some objects, particularly at high redshifts, appear to be two galaxies beginning to undergo a merger. Some also appear to have a low signal-to-noise morphology. This demonstrates the power of the asymmetry index to remove ambiguity and subjectivity in determining which galaxies are merging. While any given handful of galaxy morphologists would pick out different mergers by eye from this list, we are free from this concern as our method is purely automated and can be understood statistically.

As discussed in Conselice (2003), CAS parameters at high redshift are best used in an ensemble sense, such as finding the fraction undergoing major mergers, while any one measurement can be dominated by random errors. For example, the asymmetry values listed in Figure 7 sometimes have random errors as large as  $\delta A = 0.2$ , as do galaxies with  $A(B) < 0.35$ . These errors can remove, or add, galaxies into the merger bin, a fact that we account for in §§ 3.2 and 4.4 when analyzing the merger history of field galaxies.

## 4.2. Physical Properties of Asymmetry and Size

### 4.2.1. Asymmetries

In Figure 5 we plot the rest-frame asymmetries of our sample galaxies brighter than  $M_B < -18$  as a function of redshift and luminosity (*left*), as well as the asymmetries as a function of redshift and stellar mass for systems with  $M_* > 10^8 M_\odot$  (*right*). The symbols in Figure 5 represent the magnitude or stellar mass of each galaxy, with larger symbols representing brighter or more massive galaxies. Note that, particularly at high redshift ( $z > 1$ ), some of the galaxies consistent with mergers are relatively bright and massive.

The average asymmetries of objects brighter than the given magnitude limit listed in Table 4 are plotted in Figure 8 as a function of redshift, where the respective bright magnitude limits are labeled next to each line. The average asymmetries generally increase from the  $z = 0-1$  range to the  $z = 1-2$  range and then decreases at higher redshifts. This is especially true at the fainter magnitude limits. At brighter magnitudes the average asymmetry generally increases with redshift, peaking at  $z \sim 2.5$  and declining

TABLE 3  
MAJOR MERGER CANDIDATES IN THE HUBBLE DEEP FIELD NORTH<sup>a</sup>

NIC ID <sup>b</sup>	R.A. (J2000.0)	Decl. (J2000.0)	Redshift <sup>c</sup>	$A(B)_{\text{rest}}^d$	$M_B$	$(B-V)_{\text{rest}}$
1022.....	12 36 50.2	62 12 39.8	0.47	$0.40 \pm 0.00$	-20.62	0.50
1335.....	12 36 41.4	62 11 42.5	0.55	$0.75 \pm 0.01$	-18.70	0.71
826.....	12 36 39.7	62 12 29.4	0.83	$0.50 \pm 0.05$	-18.48	0.19
330.....	12 36 50.0	62 13 51.0	0.85	$0.64 \pm 0.03$	-19.93	0.28
40.....	12 36 48.6	62 14 23.2	0.95	$0.61 \pm 0.02$	-19.33	0.31
909.....	12 36 57.7	62 13 15.2	0.95	$0.44 \pm 0.02$	-20.46	0.33
488.....	12 36 48.6	62 13 28.3	0.96	$0.37 \pm 0.20$	-20.36	0.32
1076.....	12 36 40.8	62 12 03.1	1.01	$0.39 \pm 0.03$	-20.23	0.29
152.....	12 36 48.3	62 14 12.4	1.02	$0.37 \pm 0.02$	-19.60	0.35
1447.....	12 36 44.5	62 11 41.6	1.02	$0.37 \pm 0.02$	-20.39	0.33
1552.....	12 37 01.6	62 12 26.8	1.05	$0.67 \pm 0.01$	-18.17	0.59
576.....	12 36 49.1	62 13 21.9	1.08	$0.59 \pm 0.11$	-19.57	0.64
519.....	12 36 42.5	62 13 05.2	1.10	$0.51 \pm 0.09$	-19.37	0.39
1652.....	12 36 49.7	62 11 49.0	1.22	$0.71 \pm 0.01$	-18.25	0.33
1090.....	12 36 56.6	62 12 52.7	1.23	$0.54 \pm 0.02$	-19.70	0.36
1568.....	12 36 54.3	62 12 02.6	1.23	$0.36 \pm 0.02$	-19.67	0.54
1141.....	12 36 50.0	62 12 26.3	1.23	$0.86 \pm 0.04$	-19.49	0.37
884.....	12 36 55.2	62 13 09.0	1.27	$0.39 \pm 0.02$	-19.25	0.56
577.....	12 36 42.7	62 13 06.0	1.29	$0.41 \pm 0.16$	-20.58	0.64
872.....	12 36 51.6	62 13 00.3	1.34	$0.68 \pm 0.03$	-18.56	0.25
360.....	12 36 52.7	62 13 54.8	1.36	$0.59 \pm 0.05$	-22.17	0.27
368.....	12 36 47.4	62 13 37.2	1.41	$0.45 \pm 0.04$	-18.09	0.44
1431.....	12 36 42.7	62 11 40.8	1.44	$0.37 \pm 0.12$	-18.31	0.39
1021.....	12 36 46.2	62 12 28.5	1.45	$0.63 \pm 0.05$	-19.94	0.36
1520.....	12 37 00.8	62 12 27.6	1.50	$0.43 \pm 0.17$	-18.12	0.39
1188.....	12 36 54.0	62 12 35.2	1.50	$0.38 \pm 0.05$	-18.20	0.09
1570.....	12 36 58.1	62 12 14.3	1.51	$0.39 \pm 0.07$	-18.27	0.33
1512.....	12 36 52.1	62 12 01.2	1.53	$0.36 \pm 0.09$	-19.96	0.66
970.....	12 36 45.6	62 12 33.5	1.56	$0.65 \pm 0.17$	-18.49	0.39
1020.....	12 36 46.2	62 12 29.1	1.75	$0.84 \pm 0.06$	-19.54	0.21
422.....	12 36 43.2	62 13 19.1	1.78	$0.36 \pm 0.07$	-18.33	0.33
957.....	12 36 45.4	62 12 33.7	1.81	$0.49 \pm 0.14$	-20.12	0.51
1140.....	12 36 49.9	62 12 27.0	1.86	$0.36 \pm 0.22$	-18.92	0.35
732.....	12 36 44.4	62 12 44.1	1.98	$0.40 \pm 0.11$	-21.26	0.35
229.....	12 36 51.3	62 14 11.3	2.01	$0.46 \pm 0.15$	-20.80	0.23
466.....	12 36 53.0	62 13 44.2	2.02	$0.66 \pm 0.15$	-21.21	0.29
1583.....	12 36 54.8	62 12 03.2	2.49	$0.55 \pm 0.12$	-20.36	-0.26
1252.....	12 36 51.7	62 12 21.4	2.71	$0.63 \pm 0.03$	-21.06	0.38
604.....	12 36 44.8	62 13 07.0	2.78	$1.06 \pm 0.10$	-21.35	...
1358.....	12 36 45.3	62 11 52.2	2.80	$0.45 \pm 0.05$	-21.97	0.44
522.....	12 36 44.1	62 13 10.8	2.93	$0.36 \pm 0.04$	-22.61	...
813.....	12 36 47.9	62 12 55.4	2.93	$0.42 \pm 0.03$	-21.87	...
1541.....	12 36 48.3	62 11 45.8	2.98	$0.38 \pm 0.07$	-21.17	...

NOTE.—Units of right ascension are hours, minutes, and seconds, and units of declination are degrees, arcminutes, and arcseconds.

<sup>a</sup> These are the galaxies with rest-frame  $B$ -band asymmetries greater than 0.35 after correcting for systematic effects based on our simulations (§ 2.3.5). We also list only those systems at  $z > 2$  that are brighter than  $M_B = -20$ , as the identify of a major merger for fainter galaxies at  $z > 2$  becomes less certain, and the implied merger fraction is more of a statistical quantity.

<sup>b</sup> NIC ID is the identification number in the Dickinson et al. 2003b catalog.

<sup>c</sup> Redshifts are a mix of spectroscopic, when available, otherwise photometric.

<sup>d</sup> Rest-frame  $B$ -band asymmetries, which have been corrected for systematic redshift effects (§ 2.3.5).

thereafter. At the brightest magnitude limit of  $M_B < -22$  the average asymmetry increases greatly between  $z \sim 1$  and 1.5 and then stays large at higher redshifts.

#### 4.2.2. Colors

We can get some idea of the stellar populations that make up galaxies seen in the HDF by examining their rest-frame Johnson  $B-V$  colors. These colors are derived from an interpolation of the broadband photometry, based on the known spectroscopic redshift or computed photometric

redshift, for each object. A plot of rest-frame color versus redshift is shown in Figure 9 out to  $z \sim 2.5$ , the limit where we can measure rest-frame  $B-V$  colors. An obvious feature of this plot is the presence of a large population of faint and very blue galaxies at redshift above  $z \sim 1.5$ , which is not seen at lower redshifts. Some of these galaxies are systems with low asymmetries seen in the corresponding diagram of asymmetry versus redshift.

Many of these very blue and faint galaxies, however, are the result of either noisy photometry, imprecise

TABLE 4  
AVERAGE REST-FRAME  $B$ -BAND ASYMMETRIES AT VARIOUS MAGNITUDE LIMITS

Redshift Range	$M_B < -18$	$M_B < -19$	$M_B < -20$	$M_B < -21$	$M_B < -22$
0–1.0 .....	$0.19 \pm 0.12$	$0.21 \pm 0.12$	$0.20 \pm 0.10$	$0.16 \pm 0.06$	$0.13 \pm 0.00$
1–2.0 .....	$0.20 \pm 0.18$	$0.21 \pm 0.16$	$0.20 \pm 0.12$	$0.23 \pm 0.13$	$0.33 \pm 0.25$
2–3.0 .....	$0.15 \pm 0.19$	$0.17 \pm 0.17$	$0.23 \pm 0.18$	$0.35 \pm 0.22$	$0.28 \pm 0.07$
3–3.5 <sup>a</sup> .....	$0.14 \pm 0.19$	$0.13 \pm 0.19$	$0.16 \pm 0.18$	$0.17 \pm 0.17$	$0.33 \pm 0.19$

<sup>a</sup> At the redshift range 3–3.5 we are no longer sampling the rest-frame  $B$ -band morphologies of these galaxies but are viewing them in their near UV.

photo-zs, bad  $K$ -corrections, or a combination of these effects, as very few nearby galaxies have negative  $B-V$  colors. Population synthesis models also show that objects with mean weighted single stellar population burst ages of 50 Myr, with no subsequent star formation, have a color  $B-V \sim 0.04$  (Bertelli et al. 1994). In fact, since most of these colors are derived from spectral energy distribution fits to broadband photometry, there are likely to be some systematic errors in individual colors. We therefore only use these colors in later figures as representative ensembles in different populations. The values of these colors also do not affect any of the quantitative results of this paper. There does appear, based in Figure 9, to be an absence of bright red galaxies with  $M_B < -20$  and  $B-V > 0.5$  at  $z > 1.5$ , although we cannot rule out the possibility that some intrinsically red galaxies appear blue in Figure 9 as a result of systematic effects.

#### 4.2.3. Asymmetry and Color Evolution in the Bright Galaxy Population

The relationship between asymmetry, color and magnitude for HDF galaxies is shown by plotting rest-frame  $B$ -band asymmetries as a function of  $M_B$  into two different

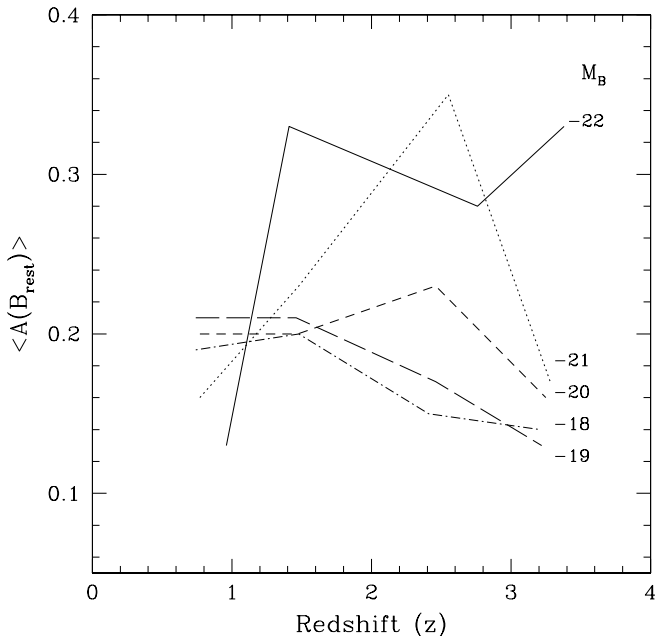


FIG. 8.—Plot of the average rest frame  $B$ -band asymmetry for galaxies at different magnitude limits as a function of redshift. Variations of these averages are listed in Table 4.

redshift bins in Figure 10. This figure shows  $M_B$  versus  $A(B)$ , where the points are colored according to their rest-frame  $B-V$ -values, within the redshift ranges  $0 < z < 1.5$  (*left*) and  $1.5 < z < 3$  (*right*), respectively. This roughly divides the sample into galaxies dominated by visible star formation and those that are not. Figure 10 (*left*) shows that the brightest galaxies in the low-redshift bin have low asymmetries and red  $B-V$  colors, consistent with smooth stellar populations, such as ellipticals. There is also a clear bifurcation in this panel, such that asymmetric galaxies are generally blue and the low-asymmetry objects are generally red (see § 4.3), the bluer objects possibly the result of merger induced starbursts. We see the opposite, however, at higher redshifts,  $1.5 < z < 3$  (*right*), where the brightest galaxies tend to be blue objects undergoing starbursts, which have high asymmetries, suggesting they are potentially major mergers.

#### 4.2.4. Size Evolution

Another property that we investigate is the size evolution of galaxies in the HDF. For this we use the  $0.5 \times k_r \times a$  radius within which asymmetries are measured. Like all the

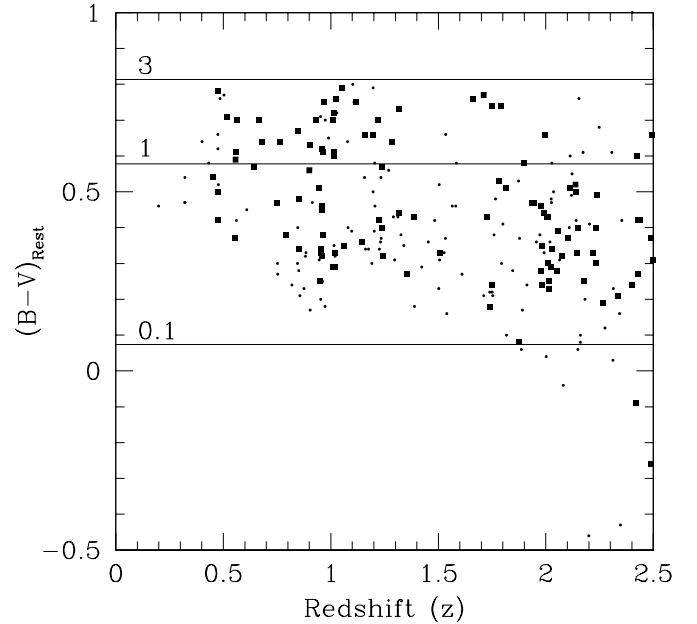


FIG. 9.—The  $B-V$  color distribution of galaxies plotted as a function of redshift ( $z$ ). The larger boxes are galaxies at  $M_B < -20$ , while the small dots are galaxies with  $M_B > -20$ . The solid lines show synthesis stellar population colors with ages of 0.1, 1, and 3 Gyr for systems that formed in bursts.

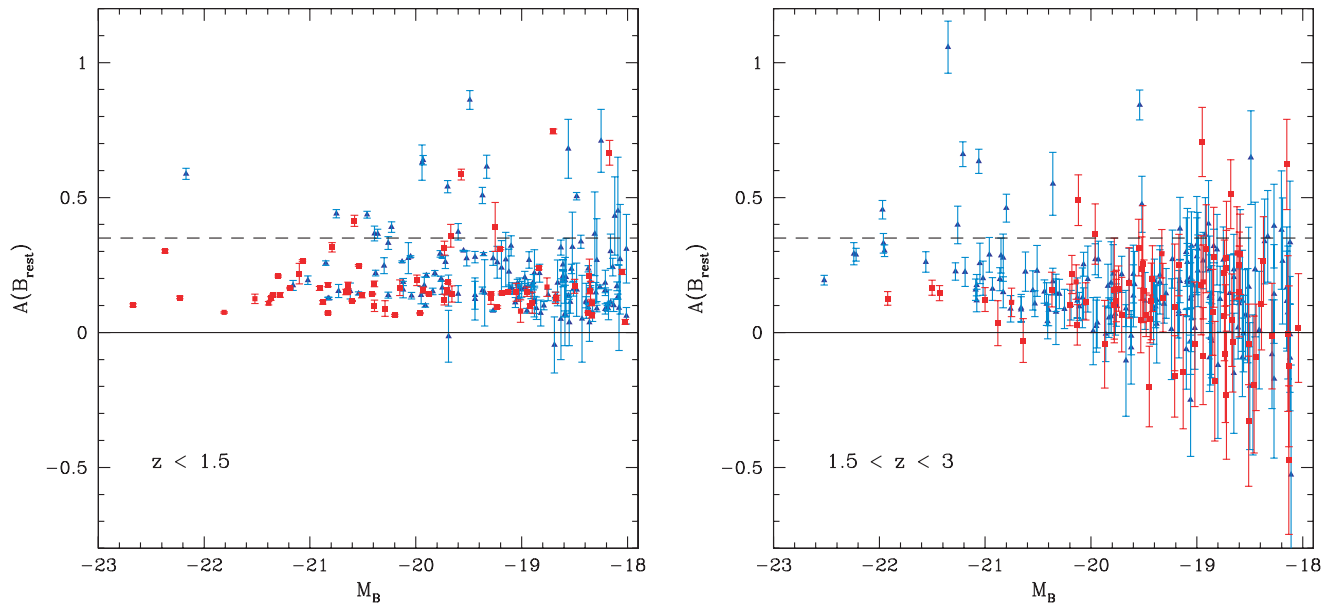


FIG. 10.—Relationship between the rest frame  $B$ -band asymmetry  $A(B_{\text{rest}})$  and absolute magnitude ( $M_B$ ) for HDF galaxies at two different redshift bins:  $z < 1.5$  and  $1.5 < z < 3$ . The color of each point is dictated by the rest-frame  $B-V$  color of each galaxy, such that blue points are systems with  $B-V < 0.5$  and red points are for galaxies with  $B-V > 0.5$ .

other parameters discussed in this paper the apparent sizes of objects depends on redshift, as dictated by the angular size distance. However, the sizes of objects may also appear smaller because of surface brightness dimming, which makes the outer parts of galaxies difficult to detect. To address this issue, we investigate (through the simulations discussed in § 2.3.5) how measured sizes of galaxies change due to cosmological surface brightness dimming. The change in galaxy sizes due to this effect are plotted in Figure 4 (*right*), where average radius differences and their  $1\sigma$  variations are plotted as a function of redshift.

When we apply this correction to the measured sizes in the rest-frame  $B$  band and examine the resulting distribution as a function of redshift, we get Figure 11. There are two interesting properties in this figure. The first is that there appears to be a lower limit on galaxy sizes, which is around 3 kpc. This limit is likely the result of the SExtractor detection method and effects from the PSF, as galaxies smaller than this certainly exist in the local universe (e.g., Conselice, Gallagher, & Wyse 2002). There is in fact a bias in the way that SExtractor measures the sizes of galaxies, which typically depends upon luminosity. Therefore, the best way to view Figure 11 is as a relative change in galaxy sizes with redshift. The range and distribution of galaxy sizes appears roughly constant between  $1.4 < z < 3$ , while for  $z < 1.4$ , there are significantly more galaxies with radii above 7 kpc. Short of a significant amount of cosmic variance, this evolution is real, as these sizes have been corrected for cosmological dimming. There therefore appear to be no galaxies at  $z > 1.4$  larger than 10 kpc in the HDF-N, even after correcting for redshift effects.

This is consistent with the idea (but does not prove it) that nearby large galaxies are forming from the mergers of lower mass and presumably smaller galaxies. An alternative interpretation is that these galaxies are still forming (inside out) from accreted intergalactic gas cooling into stars after  $z \sim 1.5$ . Size and luminosity evolution (Ellis et al. 1996)

alone do not prove that mergers are occurring in the galaxy population, but both effects are consistent with this idea. For the remainder of the paper we examine the structures of galaxies in the Hubble Deep Field and argue that mergers are increasingly common out to  $z \sim 3$ , especially for the most massive systems.

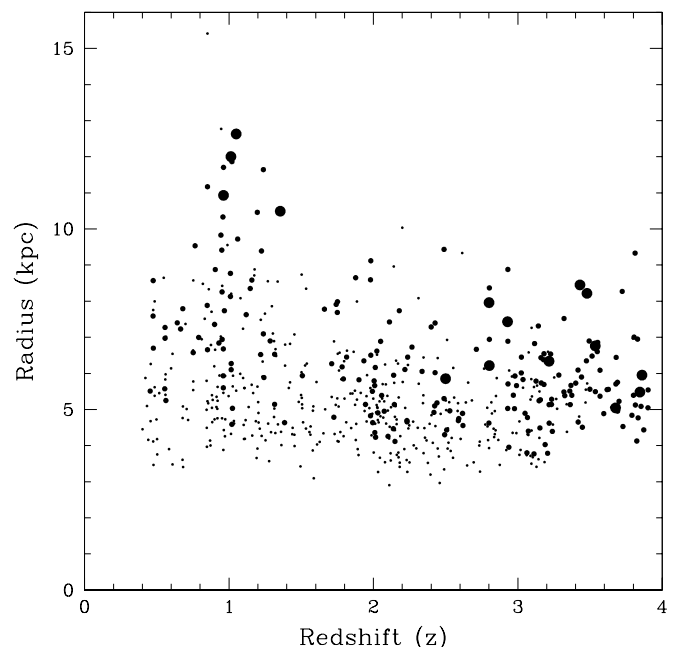


FIG. 11.—Distribution of HDF galaxy radii ( $0.5 \times k_r \times a$ ) in the rest-frame  $B$ -band to  $z < 2.5$  and observed  $H$ -band at  $z > 2.5$ , corrected for redshift effects (§ 2.3.5 and Table 1) plotted as a function of redshift ( $z$ ). The size of the symbol is proportional to luminosity, such that the smallest symbols are for galaxies with  $-20 < M_B < -18$  and the two largest symbols are for systems with  $-22 < M_B < -20$  and  $M_B < -22$ .

### 4.3. Star Formation versus Merger Formation

We can do a general test to determine if, and approximately how much, star formation is the cause of asymmetries in HDF galaxies by examining their star-forming properties as traced by color. If star formation is responsible for producing asymmetries of our sample, then we would expect more asymmetric galaxies to be dominated by star formation.

We can use the color-asymmetry diagram to investigate this question. The color-asymmetry diagram, as introduced in Conselice (1997), and discussed in CBJ00 and Conselice et al. (2000b) is a diagnostic tool that plots the disturbance of a galaxy with a measure of its spectral shape, which

signifies the ages of its stellar populations. Figure 12 shows the HDF rest-frame  $B-V$  color–rest-frame  $B$ -band asymmetry  $A(B_{\text{rest}})$  diagram plotted in bins of absolute magnitude,  $M_B$ . The differences and similarities between the local galaxy population (see CBJ00) and the HDF galaxies can be seen. The diagonal line is the relationship between asymmetry and color characterized by CBJ00 for nearby normal galaxies. The solid part is an extrapolation of this relationship to colors bluer than  $B-V \sim 0.4$ , which is typically among the bluest colors found for, e.g., dwarf irregulars in the nearby universe. While there are many galaxies with modest asymmetries and blue colors, there are few analogs of nearby ellipticals in the HDF with red colors and low asymmetries (CBJ00).

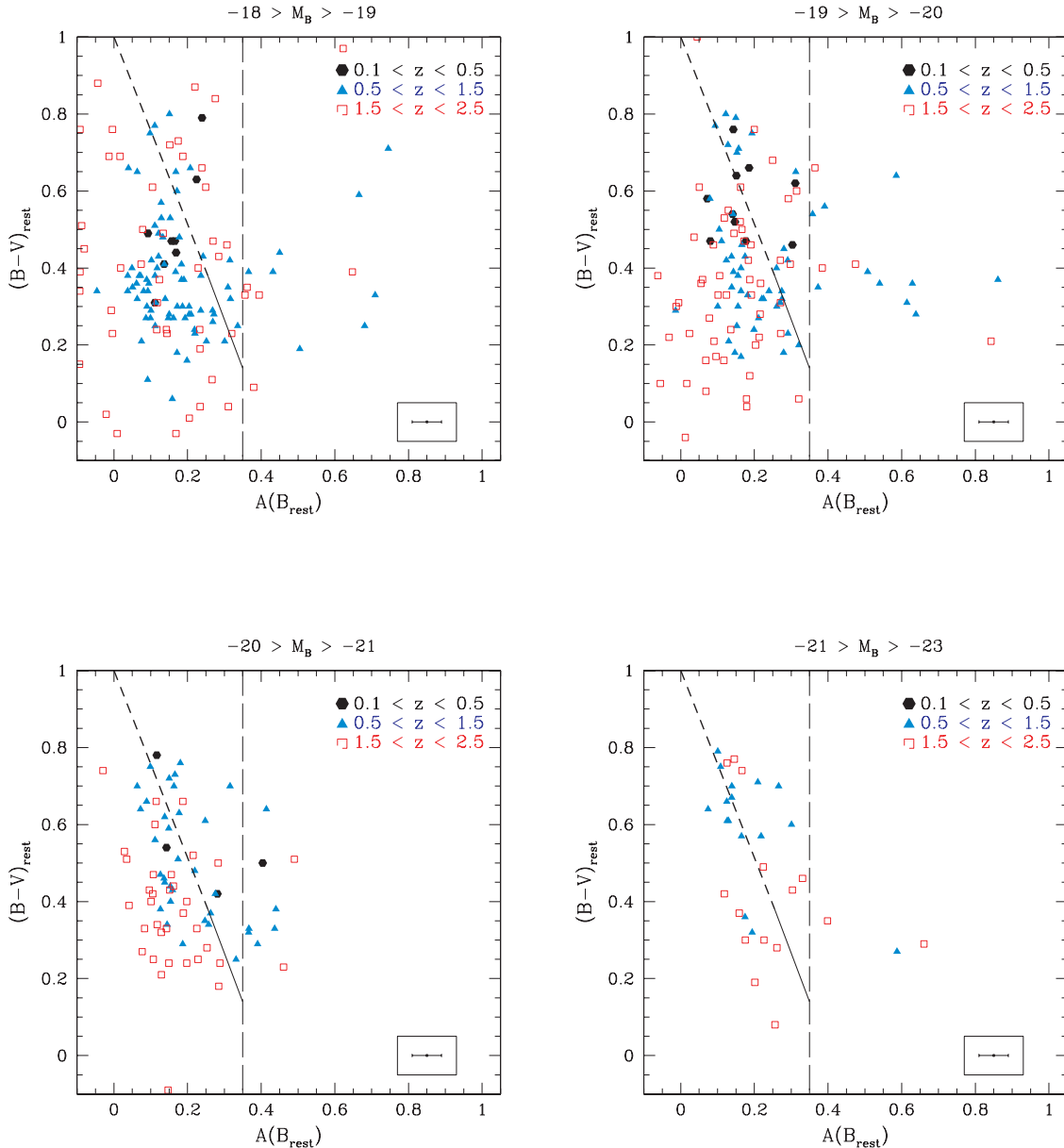


FIG. 12.—Rest-frame  $B-V$  color vs. asymmetry diagram plotted at four different luminosity intervals listed at the top of each panel. Each panel also plots galaxies divided into different redshift ranges at each luminosity. The diagonal dashed line is the relationship between  $B-V$  color and the rest-frame  $B$ -band asymmetry  $A(B_{\text{rest}})$  found for nearby normal galaxies (Conselice et al. 2000a). This line is extrapolated to bluer colors by the solid diagonal line. The vertical long-dashed line shows the  $A_{\text{merger}} = A(B-V = 0.4) + 3\sigma(B-V)$  limit we use for identifying mergers (see text).

Figure 12 can be used to argue that high asymmetries are not likely solely produced by massive amounts of star formation. At each magnitude and redshift range there exists a range of  $A(B_{\text{rest}})$  values for any given color. In fact, the galaxies consistent with mergers (those to the right of the vertical dashed line) do not have colors that significantly differ from blue nonmergers. They are, on average, bluer than the total population, but there are always galaxies with similar, or bluer, colors that do not have similarly high asymmetries (this can also be seen in Fig. 10).

If vast amounts of star formation are responsible for large asymmetries, then the galaxies with the bluest colors should have the largest asymmetries, which is clearly not the case. The galaxies with high asymmetries are unique in terms of their structure, which we interpret, for the reasons in § 3 and Conselice (2003), as an indication that they are undergoing major mergers.

#### 4.3.1. Galaxy Populations in the Color-Asymmetry Diagram

As mentioned earlier, there appears to be a lack of corresponding modern-day ellipticals, or very red symmetric objects, at any redshift bin in the HDF. This may simply be due to the fact that ellipticals are bluer at high redshift and/or due to the very small comoving volume of the HDF at low redshift, which is  $320 h^{-3} \text{ Mpc}^3$  at  $0.1 < z < 0.5$ , where few if any galaxies with  $L > L_*$  are present (Dickinson et al. (2003a, 2003b). Morphologically selected elliptical-like galaxies, however, do exist in the HDF, particularly around  $z = 1$  (Stanford et al. 2003). They are, however, bluer than nearby ellipticals, as their stellar populations are younger than those in nearby ellipticals (Menanteau et al. 1999), an effect also seen in high-redshift clusters (e.g., Dickinson 1997; Stanford, Eisenhardt, & Dickinson 1998). Passive evolution from  $z \sim 1$  to 0 will create a reddening of about 0.1 mag, which would place these symmetric bluer galaxies in the general area of nearby ellipticals (CBJ00).

Figure 12 further shows that many galaxies in the HDF are potentially undergoing mergers with asymmetries  $A(B) > 0.35$ . These objects have asymmetries inconsistent with being normal, late-type galaxies undergoing quiescent star formation, as compared with nearby galaxies. As we go to higher redshifts, the fraction of galaxies with asymmetries consistent with merging increases (Fig. 12; § 4.4).

What are the galaxies in the HDF that are not identified as mergers? At low redshifts these are simply the morphologically familiar disks and ellipticals (Fig. 7). At higher redshifts the galaxies inconsistent with merging are not readily identifiable through eyeball estimates with any specific local morphological type, but span a range, from very compact galaxies with possible “tidal” features to

diffuse bloblike systems (Fig. 7) (see also Giavalisco, Steidel, & Macchetto 1996). There are also symmetric systems at redshifts  $z > 1.5$ , although these are generally blue.

#### 4.4. Galaxy Merger Fractions and their Evolution

In this section we use the asymmetries of HDF galaxies to measure the evolution of implied major merger fractions out to  $z \sim 3$ . As in the previous sections we avoid morphological  $K$ -corrections by using the rest-frame  $B$ -band asymmetries of galaxies in the HDF and applying the corrections as needed at higher redshifts as described in § 2.3.5.

As previously described, we define a major merger as a galaxy whose rest-frame  $B$ -band asymmetry is larger than  $A_{\text{merger}} = 0.35$ , for the reasons discussed in § 3. By taking the ratio of galaxies with asymmetries  $A > A_{\text{merger}}$  to the total number of galaxies in a given parameter range, the implied merger fractions out to  $z \sim 3$  can be computed as a function of absolute magnitude  $M_B$ , stellar mass ( $M_*$ ), and redshift ( $z$ ). This allows us to determine how different galaxy types have evolved as a function of mass and time. These merger fractions are listed and plotted in four different lower galaxy absolute magnitude limits,  $M_B = -18, -19, -20, -21$ , in Table 5 and Figure 13, and mass limits  $M_* = 10^8, 10^9, 10^{9.5},$  and  $10^{10} M_\odot$  in Table 6 and Figure 14. Each merger fraction is computed for galaxies brighter, or more massive, than these limits. For example, the  $M_B = -18$  bin contains all the galaxies in the  $M_B = -19, -20,$  and  $-21$  bins.

The solid large circles in Figures 13 and 14 are the inferred merger fractions based on the asymmetry measurements using the various magnitude and mass limits shown on the panels in Figures 13 and 14. The high- and low-valued green crosses are the computed merger fractions after adding and subtracting, respectively, the  $1 \sigma$  error from each asymmetry measurement and then recalculating the merger fractions. This is a graphical representation of a likely outcome of the effect of random errors and systematic biases on the measured distribution of asymmetries (i.e., the Eddington bias) (§ 3.2).

Merger fractions from the magnitude selected pair studies of Patton et al. (1997) and Le Fèvre et al. (2000) and the kinematic pairs study of Carlberg et al. (2000) are also plotted in Figure 13 at their most representative magnitude regime. These authors compute merger fractions by finding the number of galaxies at each redshift range separated by some projected distance (usually  $< 20$  kpc), and in the case of Carlberg et al. (2000) a relative velocity difference ( $< 500 \text{ km s}^{-1}$ ). These authors, however, use various magnitude limits, and it is straightforward to compare each of these points with our values. Carlberg et al. (2000) use a magnitude limit

TABLE 5  
INFERRED MERGER FRACTIONS ( $F_{\text{merger}}$ ) AS A FUNCTION OF LUMINOSITY AND REDSHIFT<sup>a</sup>

Redshift $M_B = -18$	$F_{\text{merger}}$ -18	No. Gal. -18	Redshift -19	$F_{\text{merger}}$ -19	No. Gal. -19	Redshift -20	$F_{\text{merger}}$ -20	No. Gal. -20	Redshift -21	$F_{\text{merger}}$ -21	No. Gal. -21
0.58.....	0.04	51	0.57	0.04	26	0.59	0.07	15	0.65	0.00	4
1.10.....	0.14	142	1.10	0.18	87	1.10	0.17	41	1.10	0.08	12
1.73.....	0.14	93	1.75	0.09	53	1.84	0.10	20	1.83	0.17	6
2.41.....	0.09	183	2.46	0.10	116	2.46	0.18	56	2.55	0.4	20

<sup>a</sup> For each limiting magnitude, printed below each quantity, the fraction of galaxies consistent with undergoing a major merger is listed ( $F_{\text{merger}}$ ), as is the total number of galaxies within the redshift and magnitude limit range (No. Gal.). The redshifts listed are the averages within the limits:  $0.4 < z < 0.7$ ,  $0.7 < z < 1.3$ ,  $1.3 < z < 2$ ,  $2 < z < 3$ .

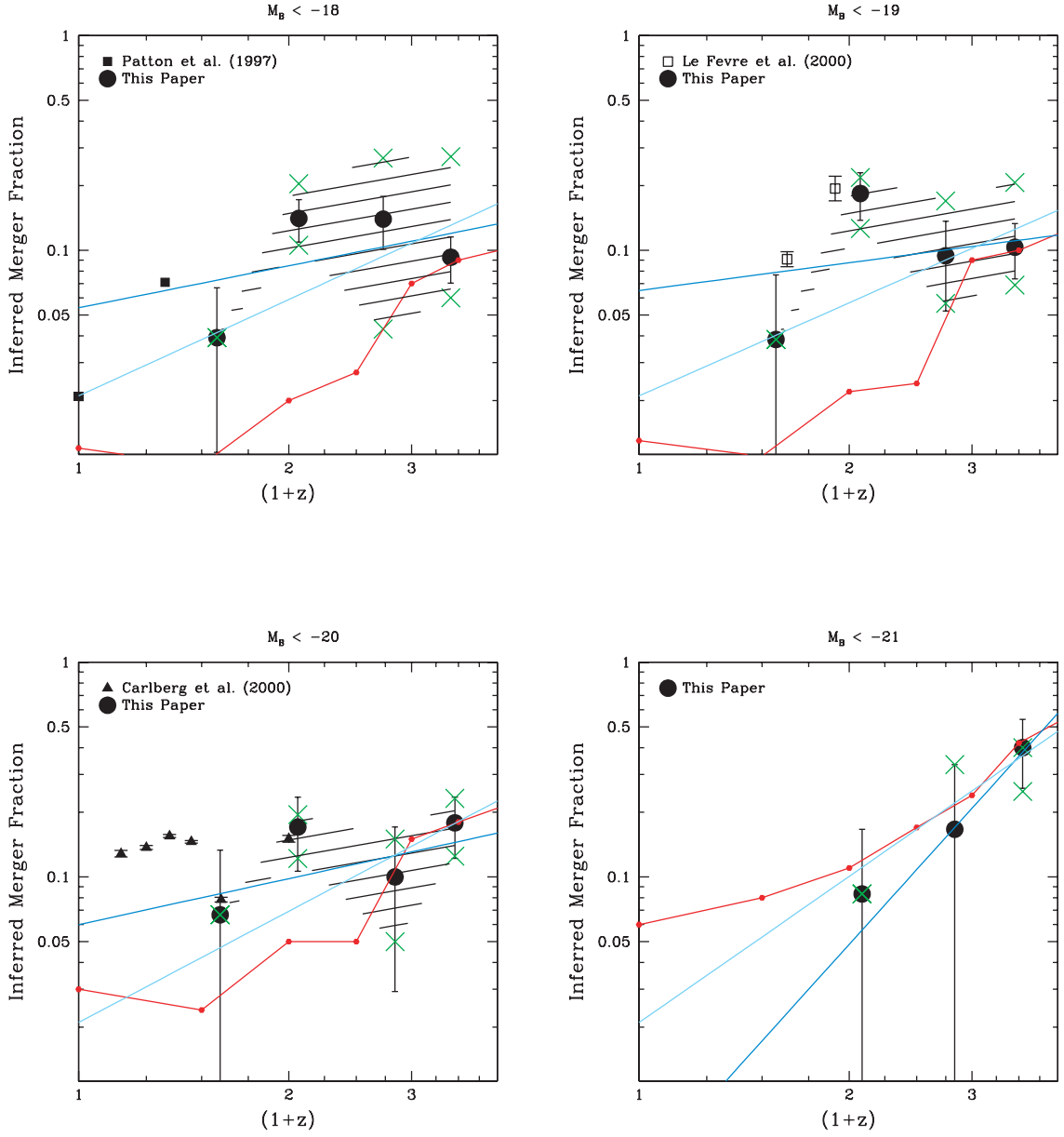


FIG. 13.—Plots of the evolution of merger fractions as a function of redshift. The solid large round symbols are merger fractions computed using the asymmetry technique. The green crosses are merger fractions computed after using the  $+1\sigma$  and  $-1\sigma$  values for each galaxy’s asymmetry. The other symbols are defined in the legend printed on each panel and are merger fractions found from galaxy pairs by Patton et al. (1997), Le Fèvre et al. (2000), and Carlberg et al. (2000). The straight blue line shows the merger fraction fit in the form  $f = f_0 \times (1+z)^{m_A}$  when only using merger fractions computed by using the asymmetry derived fractions, and the cyan line is this fit when using the asymmetry merger fractions and holding  $f_0 = 0.021$ , the  $z \sim 0$  value found by Patton et al. (1997). The solid red line and points are merger fractions selected in an analogous way from the semianalytic CDM simulation results of Benson et al. (2002).

TABLE 6  
INFERRED MERGER FRACTIONS ( $F_{\text{merger}}$ ) AS A FUNCTION OF LIMITING MASS AND REDSHIFT<sup>a</sup>

Redshift $\log(M_*) = 8$	$F_{\text{merger}}$ 8	No. Gal. 8	Redshift 9	$F_{\text{merger}}$ 9	No. Gal. 9	Redshift 9.5	$F_{\text{merger}}$ 9.5	No. Gal. 9.5	Redshift 10	$F_{\text{merger}}$ 10	No. Gal. 10
0.59.....	0.06	117	0.58	0.04	46	0.57	0.07	27	0.60	0.06	16
1.10.....	0.13	260	1.10	0.14	111	1.10	0.15	61	1.00	0.06	32
1.71.....	0.14	118	1.73	0.17	77	1.77	0.15	26	1.81	0.11	9
2.37.....	0.09	150	2.40	0.13	101	2.43	0.18	51	2.56	0.5	10

<sup>a</sup> For each limiting lower mass the number fraction of galaxies consistent with undergoing a merger ( $F_{\text{merger}}$ ) is listed as is the total number of galaxies within the redshift and magnitude limit range (No. Gal.). The redshifts listed are the averages within the limits:  $0.4 < z < 0.8$ ,  $0.8 < z < 1.4$ ,  $1.4 < z < 2$ ,  $2 < z < 3$ .

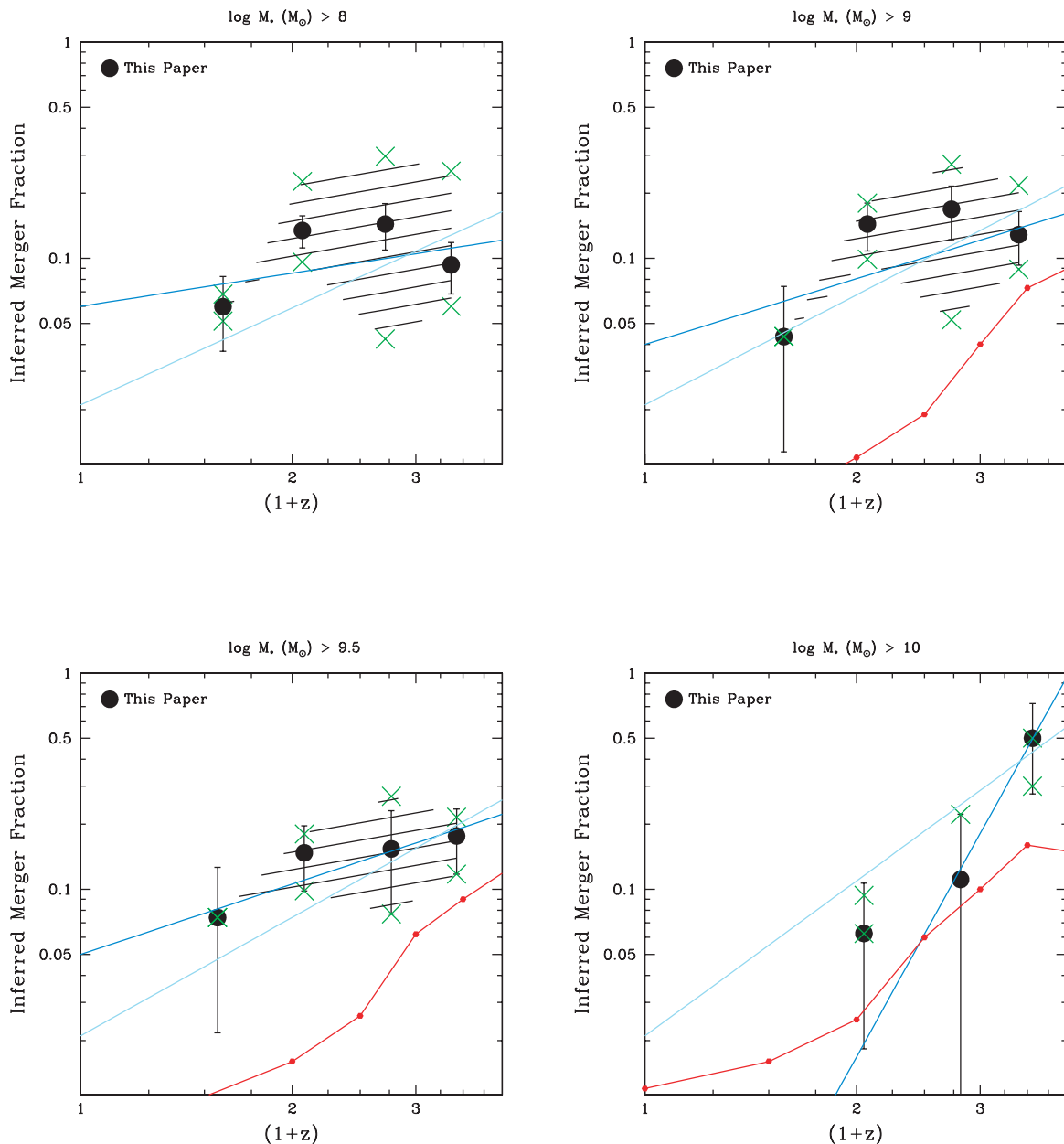


FIG. 14.—Analogous to plot of Fig. 13, except that the merger fractions are selected based on stellar mass limits rather than absolute magnitudes

of  $M_B \sim -20.5$ , while Patton et al. (1997) and Le Fèvre et al. (2000) find pairs within magnitude limits of  $M_B = -18$  and  $M_B = -19$ , respectively. None of these studies use limiting stellar masses as we do here.

Note that we may be missing a substantial number of dusty merging galaxies, such as submillimeter sources, which we are not considering because they are too faint to be detected within our limits. These would increase the merger fractions above those calculated here for galaxies within our stellar mass limits (Burgarella et al. 2003). They would not, however, effect the derived merger fractions for systems within the given magnitude limits.

#### 4.4.1. Fitting Functions

We characterize the evolution of these merger fractions by fitting a simple power-law increase with redshift:

$f_m(A, M_*, M_B, z) = f_0 \times (1+z)^{m_A}$ , where  $f_0$  is the merger fraction at  $z = 0$  and  $m_A$  is the slope of the merger fraction evolution, such that more steeply rising merger fractions have higher  $m_A$ -values. We perform these fits to quantitatively parameterize how merger fractions evolve and to compare with previous work and theoretical studies that also use this parameterization. We have fitted this model to the data in two different ways: a simple unweighted least-squares fit to all the merger fractions and by fitting the merger fractions by holding the  $z \sim 0$  point to the value found by Patton et al. (1997).

The results of these various fits are plotted as two different colored lines in Figures 13 and 14, with the fitted parameters listed in Tables 7 and 8. A fit to only the asymmetry merger fractions is shown as the straight dark blue lines in Figures 13 and 14. The  $m_A$ -values for these fits are fairly low for the

TABLE 7  
MERGER FRACTION FITS USING ABSOLUTE MAGNITUDE LIMITS<sup>a</sup>

Magnitude Limit ( $M_B$ )	Using $A$ $f_0$	Using $A$ $m_A$	$z \sim 1$ $m_A$	$z \sim 2$ $m_A$	Constant $f_0$ $f_0$	Constant $f_0$ $m_A$
-18.....	$0.06 \pm 0.05$	$0.5 \pm 0.6$	$2.5 \pm 0.3$	$2.0 \pm 0.1$	0.021	$1.5 \pm 0.2$
-19.....	$0.07 \pm 0.08$	$0.4 \pm 0.8$	$2.8 \pm 0.3$	$1.9 \pm 0.3$	0.021	$1.5 \pm 0.2$
-20.....	$0.07 \pm 0.05$	$0.7 \pm 0.6$	$2.8 \pm 0.1$	$1.8 \pm 0.3$	0.021	$1.8 \pm 0.1$
-21.....	$0.004 \pm 0.001$	$3.7 \pm 0.3$	$1.4 \pm 1.5$	$1.9 \pm 0.1$	0.021	$2.3 \pm 0.1$

<sup>a</sup> This table shows the merger fraction fitted parameters using the listed lower absolute magnitude limits ( $M_B$ ). The merger fractions are fitted in four different ways using  $f_m(A, M_B, z) = f_0 \times (1+z)^{m_A}$ . The fitted form using only the fractions computed using the asymmetries out to  $z \sim 3$  is listed in the ‘‘Using  $A$ ’’ column. The fitted merger fraction slope  $m_A$  out to  $z \sim 1$  and  $z \sim 2$  are also listed. The final two columns shows merger fraction fits when using the  $z \sim 0$  merger fraction point from Patton et al. 1997 and holding  $f_0$  to match this zero redshift point.

fainter  $M_B > -20$  (Table 7) and low stellar mass systems with  $M_* < 10^{9.5} M_\odot$  (Table 8) with typical  $m_A$ -values  $\sim 0.5$ –1. However, we find that, for the brightest and highest mass systems with  $M_B < -21$  and  $M_* > 10^{10} M_\odot$ , the merger slopes are quite steep, with values of  $3.7 \pm 0.3$  and  $5.9 \pm 1.3$ , respectively. As we argued in §§ 2 and 3.2 this increase in asymmetry between different redshifts cannot be accounted for by morphological  $K$ -corrections, detection incompleteness, systematic errors, random errors or Eddington bias.

If we use the Patton et al. (1997) merger results as a fiducial  $z \sim 0$  benchmark for all magnitude and mass cuts, and then fit the merger fraction evolution based on this, we get higher fitted slopes with values near  $m_A \sim 1.5$ –2. These fits are shown in Figures 13 and 14 as the cyan colored lines.

We can also examine the merger fraction evolution when only fitting up to certain redshifts. Tables 7 and 8 list the values of  $m_A$  for these fits out to  $z \sim 1$  and  $z \sim 2$  as a function of limiting stellar mass and magnitude. At these lower redshift limits the merger fraction slope,  $m_A$ , becomes quite steep, except for the brightest and most massive systems (Tables 7 and 8). The slopes of these fits are typically  $m_A = 2.5$ –3 for galaxies with  $M_B > -20$  or  $M_* < 10^{9.5} M_\odot$ . At  $z \sim 2$  the merger fractions are lower and the fitted slopes,  $m_A$ , decrease to  $m_A \sim 2$  for systems with  $M_B > -20$  or  $M_* < 10^{9.5} M_\odot$ . We see the opposite effect however for the most massive systems, with  $M_* > 10^{10} M_\odot$ . For these galaxies the fitted power-law slope,  $m_A$ , is quite low, between  $z \sim 0$  to 1, with a value of  $m_A = 1.7$ . The brighter systems with  $M_B < -21$  also have lower  $m_A$  slopes between  $z \sim 0$ –1 with values  $m_A \sim 1.5$ .

This bifurcation in  $m_A$ -values (Tables 7 and 8) between bright/massive and faint/lower mass galaxies suggests that

massive galaxies form from mergers much earlier than lower mass systems. The steep decline in merger fractions suggests the most massive galaxies underwent a massive merger phase in the distant past and have become the quiescent massive galaxies (or quiescent massive galaxy components) we see in the nearby universe.

#### 4.5. Merger and Stellar Mass Assembly Rates

Using further assumptions we can investigate the merger and mass accretion rates of galaxies from  $z = 0$  out to  $z \sim 3$ , or back to when the universe was only  $\sim 2.1$  Gyr old. It should be kept in mind, however, that the calculations we perform below are somewhat speculative as we do not yet have a firm understanding of many of the properties we are assuming throughout the following analysis. One possible problem with this is that the Hubble Deep Field occupies only a small volume of space and a large cosmic variance may make these results inapplicable globally. We know that in dense areas such as clusters, the merging properties are probably different than in the field (e.g., van Dokkum et al. 1999). Despite this, the Hubble Deep Field samples the high-redshift universe, and thus, within the limitations imposed by the uncertainties in our assumptions, we can compute certain evolutionary quantities for the first time.

##### 4.5.1. Merger Rates

To understand the merger and mass accretion rates, we must know the dynamical timescale and mass ratios of mergers that will result in systems with high asymmetries. That is, we have to have some idea of what type of major merger will produce a galaxy structure with an asymmetry larger than  $A_{\text{merger}}$ . The two most important parameters for

TABLE 8  
MERGER FRACTION FITS USING STELLAR MASS LIMITS<sup>a</sup>

Mass Limit [ $\log(M_*)$ ]	Using $A$ $f_0$	Using $A$ $m_A$	$z \sim 1$ $m_A$	$z \sim 2$ $m_A$	Constant $f_0$ $f_0$	Constant $f_0$ $m_A$
8.0.....	$0.07 \pm 0.03$	$0.4 \pm 0.6$	$2.4 \pm 0.1$	$2.0 \pm 0.1$	0.021	$1.5 \pm 0.2$
9.0.....	$0.06 \pm 0.03$	$0.9 \pm 0.7$	$2.5 \pm 0.3$	$2.2 \pm 0.1$	0.021	$1.7 \pm 0.1$
9.5.....	$0.06 \pm 0.01$	$0.9 \pm 0.3$	$2.6 \pm 0.0$	$2.1 \pm 0.1$	0.021	$1.9 \pm 0.1$
10.0.....	$\sim 0$	$5.9 \pm 1.3$	$1.7 \pm 0.3$	$1.6 \pm 0.1$	0.021	$2.4 \pm 0.1$

<sup>a</sup> This table shows the merger fraction fitted parameters using the listed lower stellar mass limits [ $\log(M_*)$ ]. The merger fractions are fit in four different ways using  $f_m(A, M_*, z) = f_0 \times (1+z)^{m_A}$ . The fitted form using only the fractions computed using the asymmetries out to  $z \sim 3$  is listed at the ‘‘Using  $A$ ’’ columns. The fitted merger fraction slope  $m_A$  out to  $z \sim 1$  and  $z \sim 2$  are also listed. The final two columns shows merger fraction fits when using the  $z \sim 0$  merger fraction point from Patton et al. 1997 and holding  $f_0$  to match this zero-redshift point.

understanding this are the timescale which a galaxy will remain asymmetric, such that  $A > A_{\text{merger}}$  and the mass ratios necessary to produce  $A > A_{\text{merger}}$ . The timescale for a merger also varies with redshift solely as a result of the different physical conditions of galaxies in the past, although we ignore this for the moment and assume that mergers occur within the same timescale at all redshifts.

Estimates of mass merger ratios and timescales can be computed through  $N$ -body simulations of galaxies undergoing the merging process. These simulations have been done and are fully reported in Conselice & Mihos (2003; hereafter CM03). We briefly summarize the conclusions of this study and use this information to determine the merger and mass assembly rates for galaxies seen in the HDF.

The merger of two galaxies of nearly equal mass remains asymmetric for roughly 0.9 Gyr, that is  $A > 0.35$  during this length of time (CM03). There is, however, a variation in this time range, partially for mergers between systems that do not contain similar masses. Also, we have no a priori method of determining the mass ratios of the systems that produced the galaxies that we see as mergers. To simplify this, we assume that each merger is produced from two galaxies of approximately equal stellar masses.

Using this modeled length of time as the average timescale for which  $A > A_{\text{merger}}$ , we can compute the merger rate as a function of redshift. We measure this by assuming, as earlier, that each galaxy with  $A_B > A_{\text{merger}}$  is currently undergoing a major merger that lasts for  $\sim 0.9$  Gyr, within the comoving volume between each redshift interval. Using these numbers, we can then calculate the merger rate  $\dot{\phi}_M$ , defined as the number of mergers occurring per comoving volume (in cubic gigaparsecs), divided by the timescale of the merger (0.9 Gyr).

These merger rates,  $\dot{\phi}_M$ , for galaxies brighter than  $M_B = -19$  are plotted as a function of redshift ( $z$ ) in Figure 15 as a solid line. We calculate the merger rate as  $\dot{\phi}_M = 3.9 \times 10^5$  mergers  $\text{Gpc}^{-3} \text{Gyr}^{-1}$  between  $z \sim 0.4$ – $0.8$  and find a peak rate of  $\dot{\phi}_M = 2.2 \times 10^6$  mergers  $\text{Gpc}^{-3} \text{Gyr}^{-1}$  between  $z = 0.8$  and  $1.4$ . At redshifts higher than  $z \sim 1$  the merger rate declines toward the merger rate values found at  $z < 1$ . These rates, as well as the mass accretion rates (§ 4.5.2), are listed in Table 9. From Figure 15 the merger rate appears to be nearly constant, but the merger fraction generally increases with redshift (Figs. 13–14). This difference is due to the fact that we are sampling more volume at higher redshifts, and thus the number of mergers per unit volume remains relatively flat.

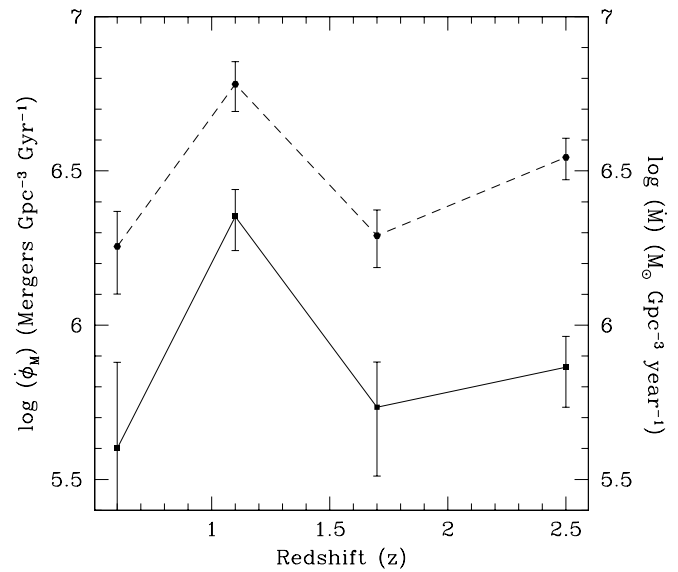


FIG. 15.—The merger rate  $\dot{\phi}_M$  in units of number of mergers  $\text{Gpc}^{-3} \text{Gyr}^{-1}$  plotted as a function of redshift ( $z$ ) (solid line) and the stellar mass accretion rate  $\dot{M}$  in units of  $M_\odot \text{Gpc}^{-3} \text{yr}^{-1}$  (dashed line) for galaxies at  $M_B < -19$ .

#### 4.5.2. Mass Accretion Rates

The stellar mass accretion rate per comoving volume ( $\dot{M}$ ) is plotted as the dashed line and on the right axis of Figure 15. The stellar mass accretion rate is computed in a similar way to the merger rate  $\dot{\phi}_M$ . It is found by assuming that each major merger with  $A > A_{\text{merger}}$  consisted previously of two galaxies of equal mass that merged. Therefore, the mass accretion rate  $\dot{M}$  is the sum of half the total mass involved in mergers in a redshift interval divided by the comoving volume in that interval, divided by the major merger time scale. The resulting  $\dot{M}$ , roughly follows the form of the merger rate with a peak value of  $6.0 \times 10^6 M_\odot \text{Gpc}^{-3} \text{yr}^{-1}$  between  $z = 0.8$  and  $1.4$ .

It may seem surprising that the mass accretion rate and merger rate track each other very well out to  $z \sim 2.5$ , since the masses of high-redshift galaxies are on average smaller than those at low redshift (Dickinson et al. 2003a, 2003b). If galaxies involved in mergers were drawn from a random distribution, then a merger rate which is constant with  $z$  would correspond to a mass accretion rate that declines with  $z$ . However, because the galaxies involved in mergers are of

TABLE 9  
MERGER AND MASS ACCRETION RATES AND DENSITIES<sup>a</sup>

Redshift Range	$\dot{\phi}_M$ (mergers $\text{Gpc}^{-3} \text{Gyr}^{-1}$ ) <sup>b</sup>	$\rho_M$ ( $M_\odot \text{Gpc}^{-3}$ ) <sup>c</sup>	$\dot{M}$ ( $M_\odot \text{Gpc}^{-3} \text{yr}^{-1}$ ) <sup>d</sup>	$\dot{M}_G$ ( $M_\odot \text{galaxy}^{-1} \text{Gyr}^{-1}$ ) <sup>e</sup>
0.4–0.8 .....	$3.9 \times 10^5$	$1.6 \times 10^{15}$	$1.8 \times 10^6$	$2.0 \times 10^8$
0.8–1.4 .....	$2.2 \times 10^6$	$5.4 \times 10^{15}$	$6.0 \times 10^6$	$4.2 \times 10^8$
1.4–2.0 .....	$5.4 \times 10^5$	$1.8 \times 10^{15}$	$2.0 \times 10^6$	$3.7 \times 10^8$
2.0–3.0 .....	$7.3 \times 10^5$	$3.1 \times 10^{15}$	$3.5 \times 10^6$	$5.5 \times 10^8$

<sup>a</sup> These merger and mass accretion rates and densities are computed for systems with  $M_B < -19$  and assuming that a major merger can be identified through the asymmetry technique for 900 Myr. For the mass accretion rate we assume that all galaxies identified as major mergers had initial masses with a 1 : 1 ratio.

<sup>b</sup> Merger rate  $\dot{\phi}_M$ .

<sup>c</sup> Mass accretion density  $\rho_M$ .

<sup>d</sup> Mass accretion rate density  $\dot{M}$ .

<sup>e</sup> Mass accretion rate  $\dot{M}_G$ .

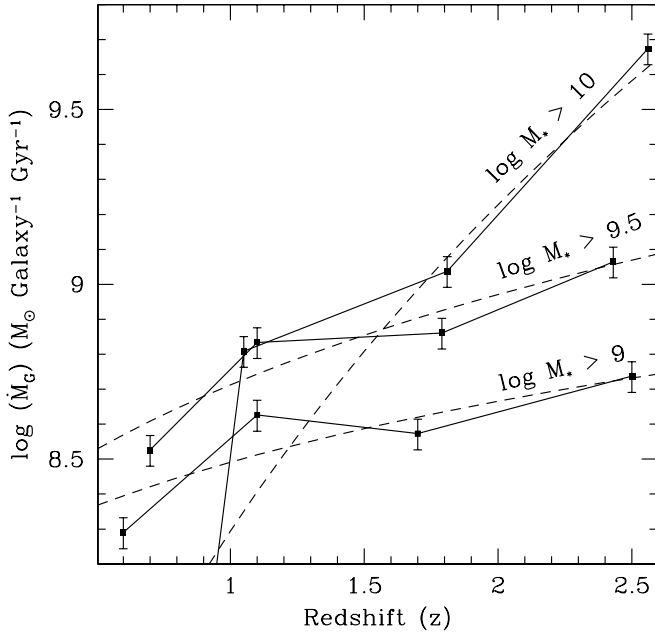


FIG. 16.—Stellar mass accretion rate per galaxy  $\dot{M}_G$ , in units of  $M_\odot$  galaxy $^{-1}$  Gyr $^{-1}$  plotted as a function of redshift ( $z$ ) for galaxies with stellar masses greater than  $10^9$ ,  $10^{9.5}$ , and  $10^{10} M_\odot$ . The dashed lines are fits to the accretion rates listed in eqs. (1)–(3).

higher mass at higher redshifts, the mass accretion rate does not decline.

The stellar mass accretion rate per galaxy  $\dot{M}_G$  is also plotted as a function of redshift in Figure 16. The values of  $\dot{M}_G$  are calculated by determining the amount of stellar mass added to galaxies from major mergers in a redshift interval divided by the total number of galaxies within that interval per merger timescale (0.9 Gyr). It is the average stellar mass accreted onto a galaxy as a result of major mergers per unit time.

The stellar mass accretion rate per galaxy,  $\dot{M}_G$ , for galaxies more massive than  $10^9$ ,  $10^{9.5}$ , and  $10^{10} M_\odot$  are plotted in Figure 16. For galaxies at  $M_* > 10^9$  the peak rate is  $5.5 \times 10^8 M_\odot$  galaxy $^{-1}$  Gyr $^{-1}$  at  $z \sim 2.5$ . The peak rate is  $1.2 \times 10^9 M_\odot$  galaxy $^{-1}$  Gyr $^{-1}$  and  $4.7 \times 10^9 M_\odot$  galaxy $^{-1}$  Gyr $^{-1}$  for systems at  $M_* > 10^{9.5} M_\odot$  and  $M_* > 10^{10} M_\odot$ , respectively. The evolution of  $\dot{M}_G$  can be further parameterized as

$$\dot{M}_G(z) = 1.6 \times 10^8 M_\odot \text{ galaxy}^{-1} \text{ Gyr}^{-1} (1+z)^{0.99 \pm 0.32} \quad (1)$$

for systems with  $M_* > 10^9$  to  $z = 2.5$ . The best fit for systems at  $M_* > 10^{9.5}$  is

$$\dot{M}_G(z) = 1.8 \times 10^8 M_\odot \text{ galaxy}^{-1} \text{ Gyr}^{-1} (1+z)^{1.47 \pm 0.25} \quad (2)$$

and

$$\dot{M}_G(z) = 5.3 \times 10^6 M_\odot \text{ galaxy}^{-1} \text{ Gyr}^{-1} (1+z)^{5.3 \pm 0.16} \quad (3)$$

for galaxies with  $M_* > 10^{10}$ . These best fits are plotted as dashed lines in Figure 16.

#### 4.5.3. Building Galaxies through Mergers

Using the derived values in § 4.5.2, we can investigate how much of the stellar mass of modern galaxies is formed through major mergers. This can be done by integrating equations (1)–(3) from  $z \sim 3$  to  $z \sim 0$  where we observe galaxies in their most evolved form. By integrating equations (1)–(3) we find that the addition of mass for these galaxies in the Hubble Deep Field North due to mergers is at most  $\sim 10^{10} M_\odot$  since  $z \sim 3$ . This shows that, on average, the most massive galaxies only slightly double in stellar mass as a result of major mergers. This is not enough stellar mass to produce an  $L_*$  galaxy at  $z \sim 0$ , which has a stellar mass of  $\sim 10^{11} M_\odot$ . However, the vast amounts of ongoing star formation in these systems, probably induced by this merging, will form stars, along with this addition of already existing stellar mass obtained through major mergers. The HDF may also be devoid of the most massive, greater than  $L_*$  galaxies, as more massive systems at  $z > 2$  do exist (Shapley et al. 2001). This is certainly a volume effect and these massive systems are rare, and the more typical galaxies found in the HDF are those that dominate the mass density.

Equations (1)–(3) reveal the first mapping of galaxy stellar mass assembly from mergers as a function of stellar mass. Combining this with star formation histories and the resulting stellar mass formation histories (Dickinson et al. 2003a, 2003b), it is possible to determine the formation histories of galaxies from  $z \sim 3$  as a function of their initial stellar mass.

#### 4.5.4. Mass and Luminosity in Mergers

We use the above information to determine the fraction of stellar mass and rest-frame  $B$ -band luminosity involved in major mergers within our stellar mass and magnitude limits, as a function of redshift. These fractions are calculated by determining the total amount of mass and light in all galaxies within a given redshift interval and comparing this with the amount of light and mass within that interval that are attached to galaxies involved in major mergers.

Figure 17 shows that roughly 5% to 25% of the stellar mass and luminosity in HDF galaxies are involved in major mergers for systems with  $M_B > -20$  or  $M_* < 10^{9.5} M_\odot$ . For the highest mass and brightest systems with  $M_* > 10^{10} M_\odot$  or  $M_B < -21$  there is a high mass fraction peak of 0.5 and a luminosity fraction peak of  $\sim 0.6$  at  $z \sim 2.5$  and a rapid decline at lower redshifts.

This again demonstrates that high mass and luminous galaxies underwent major mergers at high redshift, but are not doing so in the nearby universe. Figure 17 also shows that although the fraction of stellar mass in the brightest and most massive systems involved in major mergers declines at lower redshift, the fraction of the luminosity coming from major mergers is relatively constant until  $z \sim 1$ , when it drops. It should be kept in mind, however, that the stellar masses used to create Figure 17 are from the stars that dominate the light of these galaxies, and there is a possibility that these galaxies are hiding a significant amount of mass in the form of old stars (e.g., Papovich 2002; Dickinson et al. 2003a, 2003b). These results are, however, consistent with these massive and bright galaxies being ellipticals, or bulges formed through mergers  $\sim 9$  Gyr ago. It is also consistent with peculiar galaxies at higher redshift transforming into normal Hubble types (e.g., Driver et al. 1998; Brinchmann & Ellis 2000).

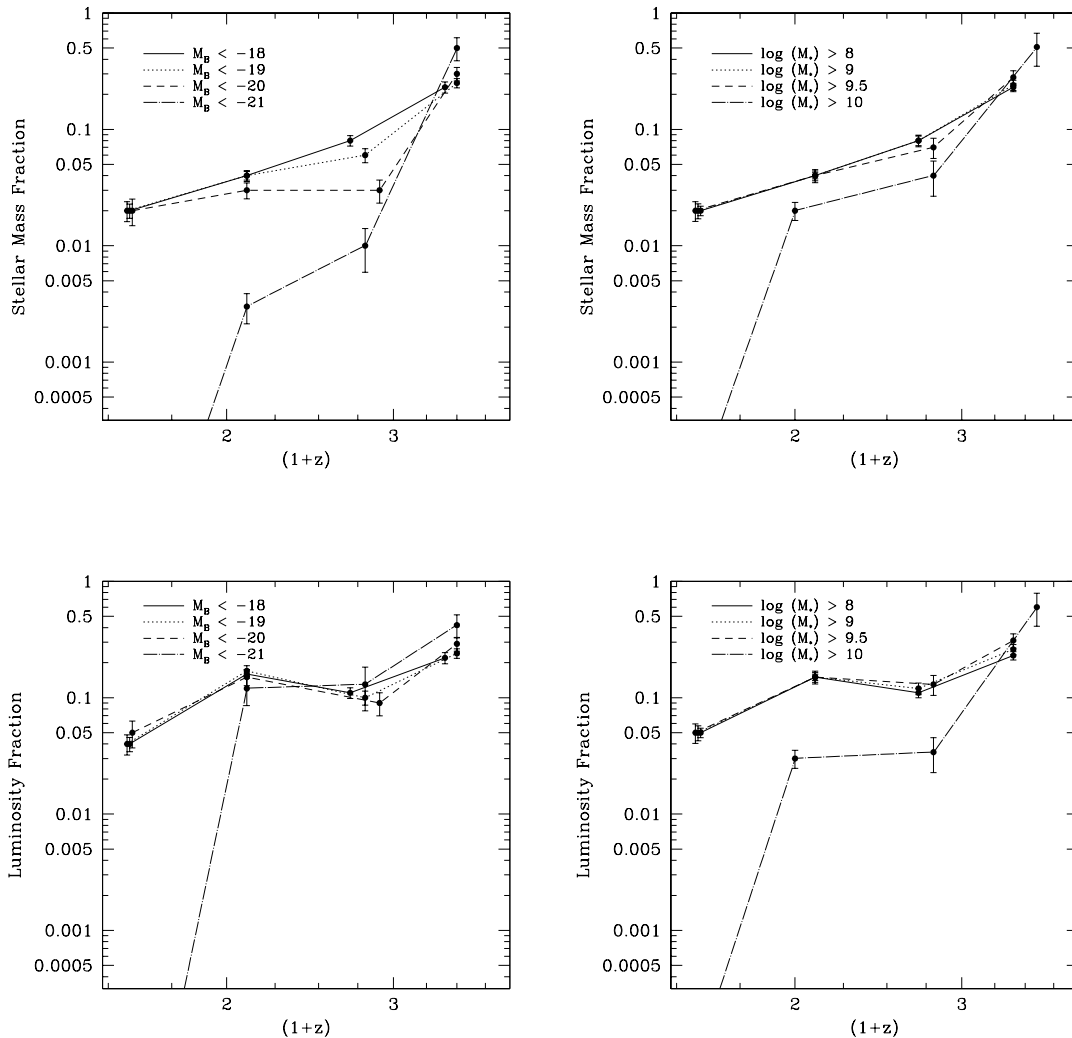


FIG. 17.—Plots of the fraction of stellar mass and galaxy luminosity involved in mergers as a function of redshift and magnitude (*left*) and stellar mass (*right*). The different lines show the fraction of mass and rest-frame  $B$ -band luminosity involved in mergers at different luminosity and stellar mass upper limits.

#### 4.5.5. Possible Biases

The evolution in Figures 16 and 17 appears steepest for objects above the largest mass threshold, i.e., greater than  $10^{10} M_{\odot}$ . Given the stellar mass evolution inferred for the general galaxy population from Papovich et al. (2001) and Dickinson et al. (2003a, 2003b), it is worth noting that a fixed mass threshold such as greater than  $10^{10} M_{\odot}$  corresponds to increasingly rare and unusual objects at higher redshifts. For example, at  $z \sim 0$ ,  $10^{10} M_{\odot}$  is  $\sim 0.1$  of the mass of an  $L_*$  galaxy, while at  $z \sim 3$  it appears to be more or less the  $M_*$  mass of Lyman-break galaxies, that is more massive objects are evidently rare. Thus, by using a fixed mass threshold, we are examining rates for objects that are increasingly extreme at higher redshift, and which (in hierarchical clustering theory) are themselves ever more strongly biased (in terms of their clustering) relative to the underlying dark matter density distribution.

This might have some implications for the results we see in Figures 16 and 17. The steepness of the apparent evolution at high masses might be an artifact due to this effect, although this is not likely the case. Unlike the mass function, the rest-frame optical luminosity function does not

evolve dramatically with redshift, and yet there still is a rapid evolution for objects with  $M_B < -21$  (Fig. 16). These bright objects, unlike galaxies with  $M_* > 10^{10} M_{\odot}$ , are not increasingly rare at higher redshift.

#### 4.6. Comparison to Models

Many papers have recently made merger history predictions based on the CDM paradigm (Khochfar & Burkert 2001; Gottlober, Klypin, & Kravtsov 2001), which we compare with our results. The idea that galaxies build up from mergers began with the modeling of this process by Press & Schechter (1974) and White & Reiss (1978). These early models traced the abundances of dark halos as a function of time with some assumptions for how galaxies form through gas cooling and feedback. Later, these models were expanded to include an initial power spectrum of dark halos assuming that dark matter is cold (White & Frenk 1991). This cold dark matter (CDM) approach using an extended Press-Schechter formalism (Bower 1991; Bond et al. 1991) has proved to be successful at reproducing many nearby and high-redshift galaxy properties through semianalytic and  $N$ -body modeling (e.g., Kauffmann, White, &

Guiderdoni 1993; Cole et al. 1994; Guiderdoni et al. 1998; Kauffmann et al. 1999; Somerville & Primack 1999; Cole et al. 2000; Somerville, Primack, & Faber 2001). However, the basic idea that galaxies and dark halos merge, the fundamental idea of CDM models, has until now never been tested observationally at high redshifts, where most galaxy formation occurs.

There are several results from this paper that we can quantitatively compare with CDM predictions of structure formation. A basic test is to examine how merger fractions change as a function of redshift in CDM models, within magnitude and stellar mass limits. Comparisons with the semianalytic model results of Benson et al. (2002) are shown in Figures 13 and 14 as solid red lines. These predicted merger fractions were computed by finding all major mergers, defined for purposes of this model as systems merging with a mass ratio of 1 : 3 or higher and within the past gigayear at a given redshift, in the semianalytic simulation of Benson et al. (2002). These are, as best as we presently know, the physical parameters within which the asymmetry index is sensitive.

These CDM merger fraction predictions agree fairly well with our computed merger fractions at the highest redshifts. At the highest masses ( $M > 10^{10} M_{\odot}$ ) and brightest magnitudes ( $M_B < -21$ ) the difference between the observed merger fractions are within 1  $\sigma$  of the Benson et al. (2002) model results at  $z > 2$ . A discrepancy is, however, present at some redshifts and at various stellar mass and magnitude limits, particularly for the faintest and lowest-mass systems. This discrepancy is highest at  $z \sim 1$  for systems with low masses ( $M_* < 10^{9.5} M_{\odot}$ ) and faint magnitudes ( $M_B > -20$ ), where we find differences at significances of greater than 3–4  $\sigma$ . At other redshifts we find that the differences are lower with significances of  $\sim 0$ –2  $\sigma$ . These differences result from the fact that, in hierarchical formation models, low-mass objects form by merging first, while it appears from our observations that lower mass galaxies tend to form continuously throughout the history of the universe, with a significant fraction of low-mass systems not undergoing mergers at any redshift.

We can also use merger fraction predictions from Khochfar & Burkert (2001) to test qualitatively how well CDM theory predicts observed merger fractions as a function of redshift, stellar mass, and absolute magnitude. Khochfar & Burkert (2001) suggest that, at brighter limits, the merger fraction power-law fits have changing  $f_0$  and  $m_A$  values, such that at higher mass and brighter magnitude limits  $f_0$  goes down, while  $m_A$  goes up. In other words, the present-day merger fraction ( $f_0$ ) is lower for more massive galaxies, while the redshift evolution of the merger rate ( $m_A$ ) is steeper. We see this from the fits to the data (Tables 7 and 8) and also in terms of the mass evolution of the galaxies we study (§ 4.4). For the most massive and brightest systems, we find that  $f_0 \sim 0$  and  $m_A \sim 4$ –6, consistent with the prediction that these massive systems formed by merging early (Khochfar & Burkert 2001).

The most interesting discrepancy between the computed merger fractions and those predicted by CDM is at a redshift of  $z \sim 1$ . Although some of the significance in the difference ( $\sim 4 \sigma$ ) can probably be accounted for by cosmic variance, we speculate that it is unlikely to account for such a high  $z \sim 1$  galaxy merger fraction. While it is possible that there exist a significant number of very low surface brightness galaxies at  $z \sim 1$ , which we are missing, we are not

likely missing normal galaxies at these redshifts, as these are clearly seen when lower redshift galaxies are placed at  $z \sim 1$ –2.5 (see § 2.3.5). We therefore conclude that, at  $z \sim 1$ , a physical effect is occurring that increases the merger fraction, or we are missing a population of galaxies for some unknown reason. The fact that CDM simulations, which have ad hoc prescriptions for creating star formation, and our merger fractions based on a small area of the sky agree in some cases so well is suggestive that at least the most massive galaxies do indeed form by mergers.

## 5. SUMMARY

In this paper we present the first direct evidence for the hierarchical assembly of massive galaxies, as well as measurements of merger and merger mass fractions and rates at redshifts  $z > 1$ . We are able to measure this evolution by identifying galaxies undergoing major mergers out to  $z \sim 3$  using the asymmetry parameter as described in Conselice et al. (2000a), which is part of the CAS morphological system (Conselice 2003). After simulating how our asymmetry measurements change due to decreased S/N and reduced resolution inherent at higher redshifts, investigating completeness, the Eddington bias, and correcting for these effects, we are able to conclude the following:

1. The merger history of field galaxies changes as a function of absolute rest-frame magnitude  $M_B$ , stellar mass ( $M_*$ ), and redshift ( $z$ ). For galaxies with  $M_B > -20$  or  $M_* < 10^{9.5} M_{\odot}$ , the merger fraction peaks at a value  $\sim 0.2$  near  $z \sim 1$  and slightly declines at higher redshift. Fitting these lower mass and fainter merger fractions to a simple power law of the form  $f = f_0 \times (1 + z)^{m_A}$ , we find power-law slopes  $m_A \sim 2.5$ –3 out to  $z \sim 1$  and  $m_A \sim 0.5$ –1 from  $z \sim 0$ –3. The corrected sizes of galaxies also become larger at lower redshifts (Fig. 11) (see also Papovich et al. 2003).

2. We see a clear bifurcation in the merger fraction evolution for the most massive,  $M_* > 10^{10} M_{\odot}$ , and brightest,  $M_B < -21$ , galaxies such that the merger fraction continues to increase for these systems at higher redshifts, with peak values near 0.5 at  $z \sim 2.5$  and low fractions  $\sim 0$  at  $z \sim 0$ . Power-law fits to the evolution of the merger fractions for these galaxies reveal very steep slopes, with  $m_A \sim 4$ –6. That is, luminous systems underwent more frequent major mergers at high redshifts than lower luminosity galaxies or their low-redshift bright and massive counterparts.

3. By using results from  $N$ -body simulations of galaxies involved in major mergers we are able to convert merger fractions into comoving volume merger rates,  $\dot{\phi}_M$ , finding a peak merger rate at  $z \sim 1$  of  $\dot{\phi}_M \sim 2 \times 10^6$  mergers  $\text{Gpc}^{-3} \text{Gyr}^{-1}$  for systems with  $M_B < -19$ .

4. Using stellar masses ( $M_*$ ) of the HDF galaxies measured by Papovich (2002) we determined the evolution in the mass accretion rate per comoving volume, the mass accretion rate per galaxy, and the fraction of mass and luminosity in galaxies undergoing major mergers as a function of redshift. We find that the peak mass accretion rate per comoving volume is  $\sim 6 \times 10^6 M_{\odot} \text{Gpc}^{-3} \text{yr}^{-1}$  at  $z \sim 1$ . We also find that the mass accretion rate per galaxy,  $\dot{M}_G$ , increases as a function of redshift for all galaxies, as does the fraction of mass in galaxies undergoing mergers. For galaxies with  $M_* > 10^9 M_{\odot}$ , we find a maximum mass per galaxy accretion rate of  $\dot{M}_G \sim 5.5 \times 10^8 M_{\odot} \text{Gyr}^{-1}$  at  $z \sim 2.5$ , with a rate evolution given by  $\dot{M}_G = 1.6 \times 10^8 M_{\odot} \text{galaxy}^{-1} \text{Gyr}^{-1} (1 + z)^{0.99 \pm 0.32}$ . The fraction of galaxy

stellar mass density involved in mergers also increases as a function of redshift, but much more rapidly and with a higher maximum fraction for the brightest and most massive systems. For galaxies with  $M_B < -21$  or  $M_* > 10^{10} M_\odot$ , the fraction of mass involved in mergers is  $\sim 0.5$  at  $z \sim 2.5$ , demonstrating that at least half of mass in the most massive galaxies in the nearby universe was involved in major mergers  $\sim 9$  Gyrs ago.

5. Qualitative and quantitative comparisons of merger fractions with results from cold dark matter simulations are in relatively good agreement for the most massive systems at  $z \sim 2.5$ . There is some discrepancy between the models and the observed merger fractions for galaxies at low masses and faint magnitudes, especially at  $z \sim 1$ . Our results are in agreement with the core result of CDM structure formation models in which massive galaxies form and evolve by merging.

Changes in the merger history through time can also explain a host of galaxy phenomenon that we have not considered or discussed in this paper, including variations in cosmic star formation history (e.g., Madau et al. 1998), the peak in density of active galactic nuclei (Boyle & Terlevich 1998), the formation of black holes (Menou, Haiman, & Narayanan 2001), and the evolution of supernovae and gamma-ray bursts. In general, our results are in agreement with the idea that major mergers have occurred in large numbers in the past and that a large fraction of the most massive galaxies in the universe have formed by the merging of lower mass systems. While our results are for only a small area of the sky, future observations with the Advanced

Camera for Surveys on the *Hubble Space Telescope*, such as the GOODS fields, will allow us to put firmer constraints on the merging history of galaxies, including determining how the merger rate varies as a function of environment.

A number of individuals have taken part in the development and acquisition of the data used in this paper. First and foremost, we thank the HDF-N NICMOS team for their contributions and tremendous work obtaining the NIR data used in this paper, including acquiring spectroscopic and photometric redshifts for galaxies in the HDF. We also thank Kirk Borne, Harry Ferguson, and Jay Gallagher for advice and suggestions regarding this work and Richard Ellis, Kevin Bundy, and Mike Santos for comments on various drafts of this paper. Andrew Benson kindly supplied his semianalytic results used here, which we greatly appreciate. This work was supported by a NSF Astronomy and Astrophysics Fellowship, and by NASA *HST* Archival Researcher grant HST-AR-09533.04-A, both to C. J. C. M. A. B. acknowledges support from NASA grants GO-9126 from STScI, which is operated by AURA, Inc., under contract NAS 5-26555; from NASA/LTSA grant NAG 5-6032; and from NSF grant AST 99-70780. M. D. and C. P. acknowledge support from NASA through grant GO-07817.01-96A, also from the STScI. Support from the University of Wisconsin-Madison, the Space Science Telescope Institute, and the California Institute of Technology during the course of this work is also gratefully acknowledged.

#### REFERENCES

- Abraham, R. G., Tanvir, N. R., Santiago, B. X., Ellis, R. S., Glazebrook, K., & van den Bergh, S. 1996, *MNRAS*, 279, L47
- Benson, A. J., Lacey, C. G., Baugh, C. M., Cole, C., & Frenk, C. S. 2002, *MNRAS*, 333, 156
- Bershady, M. A., Jangren, A., & Conselice, C. J. 2000, *AJ*, 119, 2645
- Bertelli, G., Bresson, A., Chiosi, C., Fagotto, F., & Nasi, E. 1994, *A&AS*, 106, 275
- Bertin, E., & Arnouts, S. 1996, *A&AS*, 117, 393
- Bond, J. R., Cole, S., Efstathiou, G., & Kaiser, N. 1991, *ApJ*, 379, 440
- Borne, K. D., Bushouse, H., Lucas, R. A., & Colina, L. 2000, *ApJ*, 529, L77
- Boyle, B. J., & Terlevich, R. J. 1998, *MNRAS*, 293, L49
- Bower, R. J. 1991, *MNRAS*, 248, 332
- Brinchmann, J., & Ellis, R. S. 2000, *ApJ*, 536, L77
- Broadhurst, T. J., Ellis, R. S., & Glazebrook, K. 1992, *Nature*, 355, 55
- Budavari, T., Szalay, A. S., Connolly, A. J., Csabai, I., & Dickinson, M. 2000, *AJ*, 120, 1588
- Burgarella, D., et al. 2003, in preparation
- Burkey, J. M., Keel, W. C., Windhorst, R. A., & Franklin, B. E. 1994, *ApJ*, 429, L13
- Carlberg, R. G., et al. 2000, *ApJ*, 532, L1
- Cohen, J. G., Hogg, D. W., Blandford, R., Cowie, L. L., Hu, E., Songaila, A., Shopbell, P., & Richberg, K. 2000, *ApJ*, 538, 29
- Cole, S., Aragon-Salamanca, A., Frenk, C. S., Navarro, J. F., & Jefc, S. E. 1994, *MNRAS*, 271, 781
- Cole, S., Lacey, C. G., Baugh, C. M., & Frenk, C. S. 2000, *MNRAS*, 319, 168
- Conselice, C. J. 1997, *PASP*, 109, 1251
- . 2003, *ApJS*, 147, 1
- Conselice, C. J., & Bershady, M. A. 1999, in *After the Dark Ages. When Galaxies were Young (the Universe at  $2 < z < 5$ )*, ed. S. Holt (Woodbury, NY: AIP), 225
- Conselice, C. J., Bershady, M. A., & Jangren, A. 2000a, *ApJ*, 529, 886 (CBJ00)
- Conselice, C. J., Bershady, M. A., & Gallagher, J. S. III. 2000b, *A&A*, 354, L21
- Conselice, C. J., Gallagher, J. S., & Wyse, R. F. G. 2002, *AJ*, 123, 2246
- Conselice, C. J., & Mihos, J. 2003, in preparation (CM03)
- Dawson, S., Stern, D., Bunker, A. J., Spinrad, H., & Dey, A. 2001, *AJ*, 122, 598
- Dickinson, M. 1997, in *Galaxy Scaling Relations: Origins, Evolution, & Applications*, ed. L. da Costa (New York: Springer), 215
- Dickinson, M. 1998, in *The Hubble Deep Field*, ed. M. Livio, S. M. Fall, & P. Madau (Cambridge: Cambridge Univ. Press), 219
- Dickinson, M., et al. 2000, *ApJ*, 531, 624
- Dickinson, M., Papovich, C., Ferguson, H. C., & Budavári, T. 2003a, *ApJ*, 587, 25
- Dickinson, M., et al. 2003b, in preparation
- Driver, S. P., et al. 1998, *ApJ*, 496, L93
- Eddington, A. S. 1913, *MNRAS*, 73, 359
- Ellis, R. S., Colless, M., Broadhurst, T. J., Heyl, J. S., & Glazebrook, K. 1996, *MNRAS*, 280, 235
- Ferguson, H. C., Dickinson, M., & Williams, R. 2000, *ARA&A*, 38, 667
- Giavalisco, M., Steidel, C. C., Macchetto, F. D. 1996, *ApJ*, 470, 189
- Glazebrook, K., Ellis, R., Santiago, B., & Griffiths, R. 1995, *MNRAS*, 275, 19L
- Gottlober, S., Klypin, A., & Kravtsov, A. V. 2001, *ApJ*, 546, 223
- Guiderdoni, B., Hivon, E., Bouchet, F. R., & Maffei, B. 1998, *MNRAS*, 295, 877
- Ibata, R. A., Lewis, G. F., Irwin, M. J., & Quinn, T. 2002, *MNRAS*, 332, 915
- Kauffmann, G., White, S. D. M., & Guiderdoni, B. 1993, *MNRAS*, 264, 201
- Kauffmann, G., Colberg, J. M., Diaferio, A., White, S. D. M. 1999, *MNRAS*, 303, 188
- Khochfar, S., & Burkert, A. 2001, *ApJ*, 561, 517
- Le Fèvre, O., et al. 2000, *MNRAS*, 311, 565
- Lilly, S. J., Le Fèvre, O., Crampton, D., Hammer, F., & Tresse, L. 1995, *ApJ*, 455, 50
- Lilly, S. J., Le Fèvre, O., Hammer, F., & Crampton, D. 1996, *ApJ*, 460, L1
- Madau, P., Pozzetti, L., & Dickinson, M. 1998, *ApJ*, 498, 106
- Menanteau, F., Ellis, R. S., Abraham, R. G., Barger, A. J., & Cowie, L. L. 1999, *MNRAS*, 309, 208
- Menou, K., Haiman, Z., & Narayanan, V. K. 2001, *ApJ*, 558, 535
- Newberg, H. J., et al. 2002, *ApJ*, 569, 245
- Neuschaefer, L. W., Im, M., Ratnatunga, K. U., Griffiths, R. E., & Casertano, S. 1997, *ApJ*, 480, 59
- Noguchi, M. 2000, *MNRAS*, 312, 194
- Papovich, C. 2002, Ph.D. thesis, Johns Hopkins Univ.
- Papovich, C., Dickinson, M., & Ferguson, H. C. 2001, *ApJ*, 559, 620
- Papovich, C., Dickinson, M., Giavalisco, M., Conselice, C. J., & Ferguson, H. C. 2003, in preparation
- Patton, D. R., Pritchet, C. J., Yee, H. K. C., Ellingson, E., & Carlberg, R. G. 1997, *ApJ*, 475, 29

- Patton, D. R., Carlberg, R. G., Marzke, R. O., Pritchett, C. J., da Costa, L. N., & Pellegrini, P. S. 2000, *ApJ*, 536, 153
- Petrosian, V. 1976, *ApJ*, 209, L1
- Press, W. H., & Schechter, P. G. 1974, *ApJ*, 187, 425
- Schade, D., Lilly, S. J., Crampton, D., Hammer, F., Le Fèvre, O., & Tresse, L. 1995, *ApJ*, 451, L1
- Schweizer, F., & Seitzer, P. 1988, *ApJ*, 328, 88
- Shapley, A., Steidel, C. C., Adelberger, K. L., Dickinson, M., Giavalisco, M., & Pettini, M. 2001, *ApJ*, 562, 95
- Somerville, R. S., & Primack, J. R. 1999, *MNRAS*, 310, 1087
- Somerville, R. S., Primack, R., & Faber, S. M. 2001, *MNRAS*, 320, 504
- Stanford, S. A., Eisenhardt, P. R., & Dickinson, M. 1998, *ApJ*, 492, 461
- Stanford, S. A., et al. 2003, in preparation
- Tolman, R. C. 1930, *Proc. Natl. Acad. Sci.*, 16, 511
- van Dokkum, P. G., Franx, M., Fabricant, D., Kelson, D. D., & Illingworth, G. D. 1999, *ApJ*, 520, L95
- White, S. D. M., & Rees, M. J. 1978, *MNRAS*, 183, 341
- White, R. E., & Frenk, C. S. 1991, *ApJ*, 379, 52
- White, R. E., III, Keel, W. C., & Conselice, C. J. 2000, *ApJ*, 542, 761
- Williams, R., et al. 1996, *AJ*, 112, 1335
- Wu, W., & Keel, W. C. 1998, *AJ*, 116, 1513
- Zaritsky, D., & Rix, H.-W. 1997, *ApJ*, 477, 118
- Zepf, S. E., & Koo, D. C. 1989, *ApJ*, 337, 34